Adaptive Feedforward Cancellation of Sinusoidal Disturbances in Superconducting Radio Frequency Cavities

By

Tarek Hamdi Kandil

A THESIS

Submitted to
Michigan State University
in partial fulfillment of the requirements
for the degree of

MASTER OF SCIENCE

Department of Electrical and Computer Engineering

2005

ABSTRACT

Adaptive Feedforward Cancellation of Sinusoidal Disturbances in Superconducting Radio Frequency Cavities

By

Tarek Hamdi Kandil

A control method, known as adaptive feedforward cancellation (AFC), is applied to damp sinusoidal disturbances due to microphonics in superconducting radio frequency (SRF) cavities. AFC provides a method for damping internal and external sinusoidal disturbances with known frequencies. It is preferred over other schemes because it uses rudimentary information about the frequency response at the disturbance frequencies, without the necessity for an analytic model (transfer function) of the system. It estimates the magnitude and phase of the sinusoidal disturbance inputs and generates a control signal to cancel their effect. AFC, along with a frequency estimation process, is shown to be very successful in the cancellation of sinusoidal signals from different sources. The results of this research may significantly reduce the power requirements and increase the stability for lightly loaded continuous-wave SRF systems.

To my parents, Hamdi and Hana

and to my siblings, Amro and Dahlia

ACKNOWLEDGMENTS

TABLE OF CONTENTS

LIST OF TABLES

LIST OF FIGURES

CHAPTER 1

Introduction

Control of the resonant frequency of superconducting radio frequency (SRF) cavities is required in view of the narrow bandwidth of operation. Detuning of SRF cavities is caused mainly by the Lorentz force (radiation pressure induced by the high RF field) and microphonics (mechanical vibrations) [15, Chapter 19]. In continuous-wave (cw) accelerators, microphonics are the major concern [15, Chapter 19]. It is natural to think of using fast mechanical actuators to compensate for microphonics, i.e., attenuate the effect of mechanical vibrations on detuning. This concept was applied successfully by Simrock et al [19] to a simple quarter wave resonator (QWR) with a fast piezoelectric tuner. However, the high-gain feedback approach used in [19] is too complex to apply to multi-cell elliptical cavities, which are the subject of this work. In fact, in a previous work by Simrock [12] for elliptical cavities it is stated that "the large phase shift over this frequency range makes it clear that feedback for microphonics control using the RF signal will not be possible with the piezo actuator." To date, there has been no demonstration of microphonics control on multi-cell SRF cavities, and the current thesis presents the first such demonstration.

In Chapter 2, a brief discussion of SRF cavities and different sources of detuning

is given. We formulate the microphonics control problem from a control theory viewpoint and explore various standard control approaches. The measured spectrum of cw systems in a reasonably quiet environment, as is the case with properly designed accelerators, only exhibits limited narrowband sources (sinusoidal signals) of noise. It will be shown that the AFC is the most appropriate for the task as it handles sinusoidal disturbances. AFC is developed for stable systems, as in the current case, and it does not require an analytic model of the system to design a feedback controller. In Chapter 3, we review the main elements of the theory of AFC, and in Chapter 4, we present our experimental demonstration of the successful use of AFC in microphonics control of elliptical cavities.

CHAPTER 2

Background

The Rare Isotope Accelerator (RIA) is a proposed Linear Accelerator (linac) that is designed for accelerating heavy ions that would provide 400 MeV/neucleon beams with power up to 400 kW. The driver linac is designed to accelerate any stable isotope from hydrogen to uranium, onto production targets that typically consists of heavy elements, which would produce a broad assortment of exotic isotopes. As shown in Figure 2.1, after the acceleration of isotopes onto a production target, the projectile
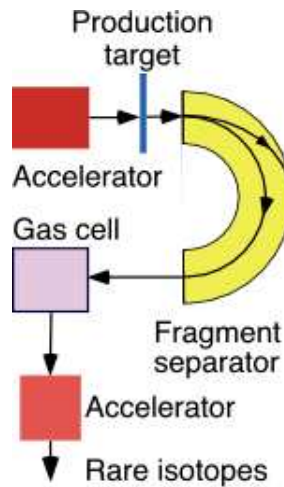
Figure 2.1. Rare Isotope Production Process.

fragments, or any light particles ejected as the result of bombardment, pass through

a fragment separation process; then the rare atoms are captured in a gas (helium) chamber in which they get ionized, re-accelerated, and delivered to different experiments for the purpose of studying their properties. Rare Isotopes are very different from the stable nuclei found on earth. The study of the exotic nuclei could help in answering many questions about how stars live and die and what is the origin of elements in cosmos. It can also lead to an understanding of the origin of the elements that constitute the earth and universe, as well as many other questions. By studying the properties of those new isotopes, an entire arena for new medical and industrial applications could be created, such as cancer treatments, and advancements in imaging tools for medical use.

The driver linac for RIA is about 500 m long, divided into two sections, the first section uses low beta (beta is the ratio between the particle velocity and speed of light) RF resonators that operate at frequencies ranging from 60-350 MHz, while the second section uses high beta resonators operating at 805 MHz, which are typically multi-cell elliptical cavities that may range from 1-9 cells. Figure 2.2 shows a 6-cell RF cavity on which this research study has been conducted.

2.1   Particle Acceleration

The RF field inside the cavity is composed of both electric and magnetic fields that are transverse waves. The charged particles are to be accelerated along the axis of the cavity, and therefore we require the electric field to be coaxial with the cavity, thus having the magnetic field transverse to the cavity axis. The most common and

Figure 2.2. A 6-cell Niobium RF cavity.

simplest transverse magnetic (TM) mode used for acceleration that satisfies these requirements is TM_{010} where the electric field is constant and travelling along the cavity axis, in this case its intensity decreases by moving away from the axis. On the other hand, the magnetic field is zero at the axis and increases by moving radially away from the axis.

Now consider that half the wavelength of the RF field is equal to the length of one cavity cell that is operating in π mode, where π mode means that the cavity is operating at a certain frequency such that it produces a 180° (π) phase shift between adjacent cells. Since the charged particles are moving at a very high speed close to the speed of light, if a negative charged particle is injected into the first cell of the cavity when the RF field has just become positive, then the field will not change direction during the transit time of the particle through the half wavelength sized cell, and thus accelerating it through the first cell. When the particle enters the second cell, the RF field has now completed the positive cycle and started the negative cycle,

5

but since the cavity is operating in the π mode, this means the field experienced a 180° phase shift inverting the field back to the positive cycle, hence accelerating the particle again.

The energy qV gained by a particle, depends on both the particle charge and the electric field voltage V_{cav}. Therefore to control the acceleration process, it is necessary to keep the magnitude and phase of the cavity voltage at known set points. An RF controller is needed to maintain accurate magnitude and phase for V_{cav}, which will be discussed in the next chapters.

2.2   Niobium Cavity Fabrication and properties

A typical cavity generates a potential of over 1 million volts. A traditional copper cavity dissipates as high as 1 million watts in the cavity walls. An SRF cavity on the other hand, dissipates about 100,000 times smaller power than that of a copper cavity. Therefore, SRF cavities are used. To have SRF cavities, we need special material and extremely cold temperature. Niobium sheets of 4 mm are used with a nominal Residual Resistivity Ratio (RRR) of 250 [6] at temperature of about -456 F or 2 Kelvin (K), where

$$\text{RRR} = \frac{\text{resistivity at 300K}}{\text{residual resistivity at low temperature (normal state)}} \qquad (2.1)$$

and higher RRR provides the best insurance against thermal breakdown.

High-grade niobium is a soft metal, which is easily fabricated, and the high purity of the sheet niobium has a reasonably high thermal conductivity, and can be electron

beam welded without introducing excess RF losses at the welded parts. The purity is not considered only in terms of bulk purity, but also in terms of inclusions from manufacturing steps, as they act as normal conducting sites for thermal breakdown of superconductivity. Therefore, the niobium sheet is scanned initially for defects by eddy-current scanning [2]. Other impurities, such as dissolved interstitial oxygen, carbon, nitrogen, and hydrogen, act as scattering sites for the electrons, which lower the thermal conductivity and enhance the chances of a thermal breakdown [14]

Cavities have been fabricated from sheet niobium by first deep draw or spin half-cells. The half-cells are then electron beam welded under vacuum. Chemical etching to a depth of 100-200 μm is done to the internal surface of the cavity to remove mechanically damaged layers for best RF performance. The cavity is then placed in a vacuum furnace for 10 hours at 600°C, 10.6 torr to prevent it from the Q degradation, where Q is the quality factor of the cavity [6]. Following that it is rinsed with ultra-pure water at high pressure to get rid of dust particles since microscopic particles stuck to the surface of the cavity can degrade its high-field performance. The foregoing processing takes place in a clean room of class 100 or better, which means that the air must be filtered to have fewer than 100 particles larger than 1 μm in size in a volume of 100 cu.ft.

2.3   Modelling the RF Cavity and Cavity Voltage

The starting point in microphonics control is to develop a mathematical model that describes how the mechanical vibrations and the control actuator determine the cavity

detuning. To obtain such a model, the cavity's frequency response is determined first. The cavity's frequency response is generated using an RF voltage network analyzer (VNA) that is connected directly to the cavity's input current and output voltage. The network analyzer sweeps the input frequency about the RF resonance, then compares the output signal of the cavity to the input signal. Figure 2.3 shows the transmitted RF amplitude and phase of the cavity at 2 K swept with the VNA, where the frequency at which the gain response peaks is called the eigenfrequency or
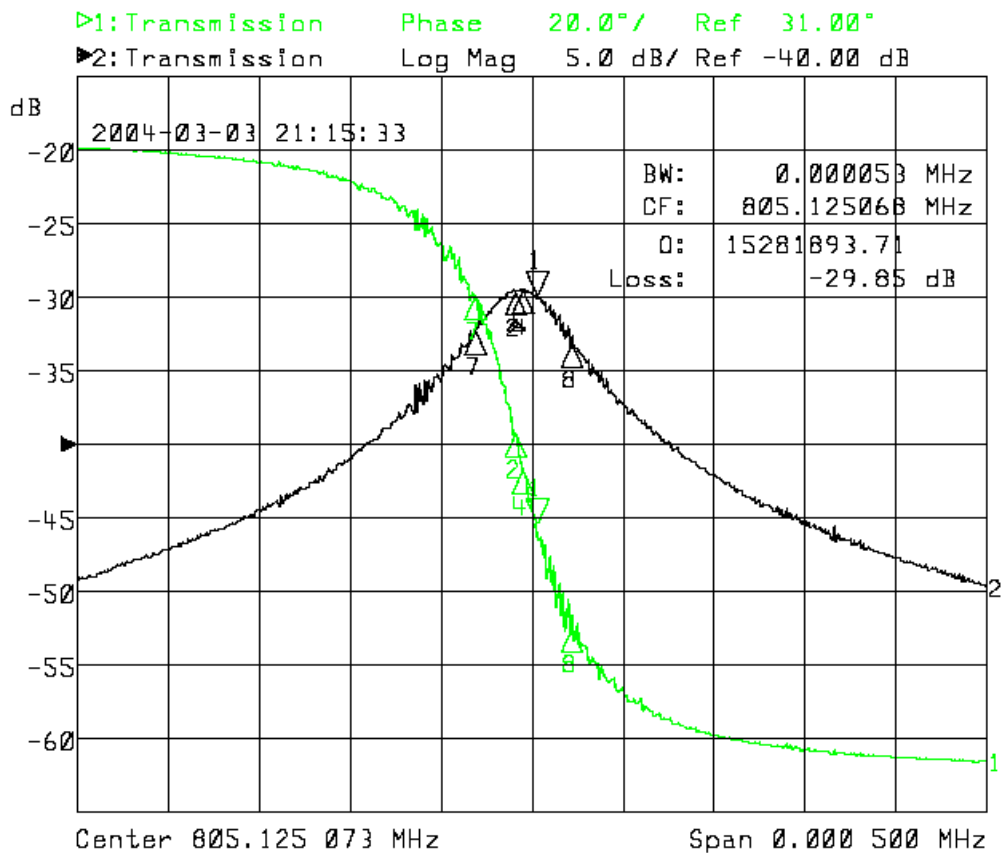
Figure 2.3. Transmitted RF response of the cavity at 2 K.

resonance frequency of the RF cavity. Ideally when no disturbance is present, the

eigenfrequency should be at 805 MHz, with a zero phase at that frequency. It is easily noticed that the frequency response shown in Figure 2.3 is similar to that of a parallel RLC circuit, hence it is shown in [17, Section 3.2] that the relationship between the cavity detuning $\Delta\omega = \omega_0 - \omega$ and the phase angle ψ (between the driving current and cavity voltage) can be approximated at steady state by

$$\tan\psi = 2Q_L\left(\frac{\Delta\omega}{\omega}\right) \tag{2.2}$$

where ω is the RF generator frequency, ω_0 is the cavity eigenfrequency, and Q_L is the loaded Q factor, defined by

$$Q_L = 2\pi \cdot \frac{\text{Stored energy}}{\text{Total power dissipation/cycle}} \tag{2.3}$$

2.4 Detuning in RF Cavities

Since the SRF cavity is cooled down to 2 K and is made of thin niobium sheet (4 mm thick), the cavity shape is susceptible to changes due to any force that might act on it. As stated earlier in the introduction, detuning of SRF cavities is caused mainly by Lorentz force and microphonics.

2.4.1 Lorentz Force Detuning

To have a more effective acceleration of the charged particles, it is desired to increase the electromagnetic fields in the superconducting structure. However high fields in
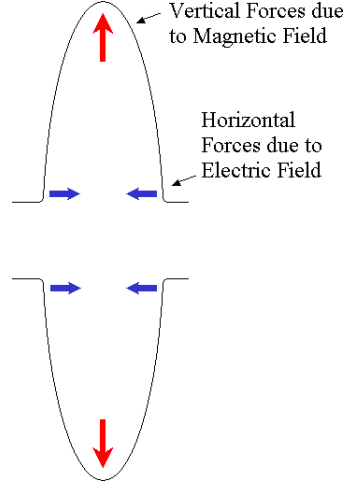
Figure 2.4. Radiation pressure (Lorentz forces) shown acting on a single cell cavity.

the cavity cause radiation pressure known as Lorentz forces acting on the walls as shown in Figure 2.4 This radiation pressure is given by [17]

$$P_s = \frac{1}{4}(\mu_0|\overrightarrow{H}|^2 - \epsilon_0|\overrightarrow{E}|^2) \tag{2.4}$$

where $\overrightarrow{E}$ and $\overrightarrow{H}$ are the electric and magnetic fields acting on the cavity walls. This pressure exerted on the walls causes some deformation in the cavity's shape and consequently a change in the resonator's volume by ΔV. In this case the eigenfrequency is shifted by a volume change according to the following relation given in [17]:

$$\frac{\omega_0 - \omega}{\omega_0} = \frac{\int_{\Delta V}(\epsilon_0|\overrightarrow{E}_0|^2 - \mu_0|\overrightarrow{H}_0|^2)dV}{\int_V(\epsilon_0|\overrightarrow{E}_0|^2 + \mu_0|\overrightarrow{H}_0|^2)dV} \tag{2.5}$$

where $\overrightarrow{E}_0$ and $\overrightarrow{H}_0$ are the unperturbed fields.

It is shown in Figure 2.4 that electric field causes axial contraction of the cell (negative change), while the magnetic field causes radial expansion (positive change).

10

Both changes yield a decrease in the resonance frequency, as shown by Equation (2.5). However, operating in a continuous-wave mode rather than operating with a pulsed accelerating field causes the Lorentz force to be insignificant, in addition to having stiffening rings that are used to reduce radiation pressure effect along with having relatively thick walls of 4 mm, which enhances the rigidity, yet is thin enough to ensure the effectiveness in the cooling process as well as keeping a lower material costs. Therefore our major concern is microphonics disturbances.

2.4.2 Microphonics Detuning

As mentioned in the previous subsection, microphonics is the main cause of detuning since the accelerator is operating in cw. Mechanical vibrations are always present and appear in an uncorrelated manner. Possible sources of microphonics along with the transfer medium are shown in Figure 2.5. However, not all of these sources are considered potential disturbances since a properly designed accelerator would be in reasonably quite environment and adequately isolated from ground.

Effect of Detuning

As mentioned earlier in Section 2.1, the energy gained by a particle to be accelerated depends on both the particle charge and the cavity voltage. Therefore, keeping the voltage constant is a very important matter. Figure 2.6 [17] shows the cavity's response under three different conditions. The first curve (1) shows the response of the cavity under the desired operating conditions when the resonator is initially excited at resonance at the desired cavity voltage with zero phase ($\psi = 0$). Curve (2) shows
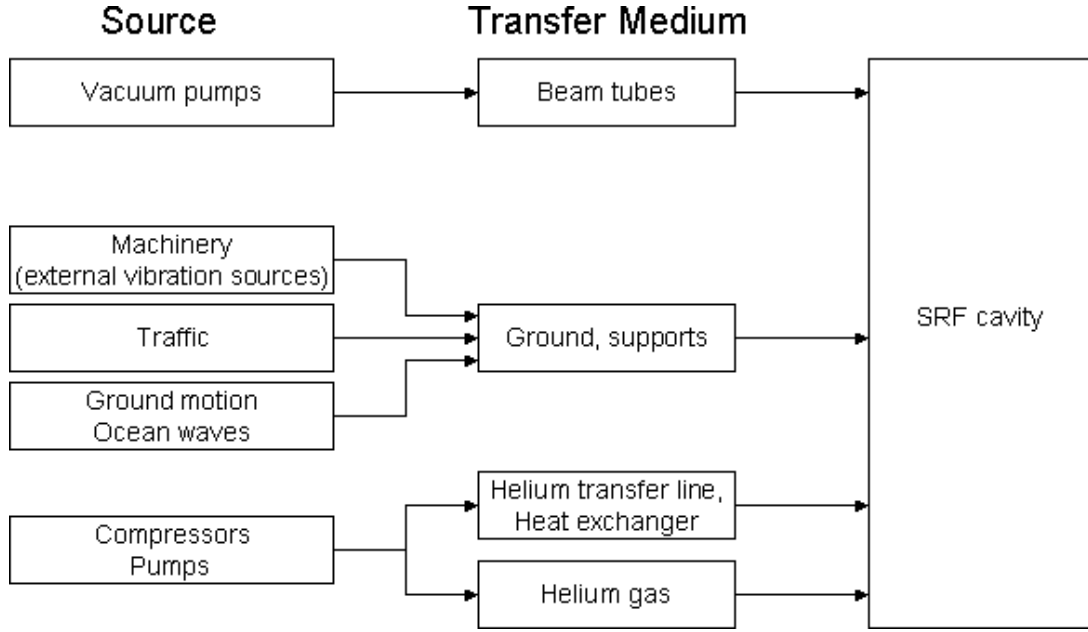
Figure 2.5. Possible sources and transfer mediums for microphonics [17].

the case when a disturbance is present that deforms the cavity walls and causes a shift in the eigenfrequency of the cavity, hence operating at the same frequency results in a voltage decrease as well as a phase shift ($\psi \neq 0$). One way to compensate for this change is to increase the RF power together with shifting the phase of the driving signal in an opposite direction, and this is illustrated on the figure by curve (3), which shows that despite of the shift in the eigenfrequency of the cavity, we still get the desired voltage level with a zero phase.

2.4.3 Different Methods for Microphonics Mitigation

Electronic Compensation

This method is shown in curve (3) of Figure 2.6. Although it is considered one way of solving the problem, increasing the power is not considered a practical solution due
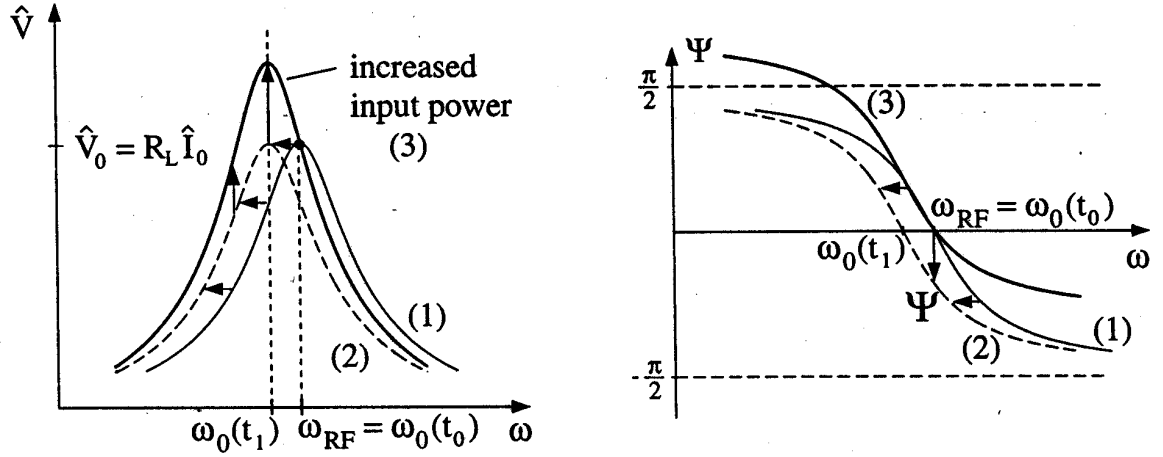
Figure 2.6. Transfer function of SRF Cavity. The left plot shows the magnitude response, where $\hat{V}$ is the cavity voltage, while the right plot shows the phase response, where ψ is the phase angle between the driving current and the cavity voltage. A disturbance causes the magnitude to change from curve (1) to curve(2) resulting in a decrease in the amplitude, which is then compensated in curve (3) by an increase in the input power along with a phase shift in the opposite direction [17].

to the high cost of this operation.

Structural Modification

Cavities typically have very thin walls and are susceptible to deformation easily; hence using thicker sheets for the walls has been considered. As mentioned in Section 2.2, 4 mm niobium sheets were used, which are relatively thick compared to some other cavities ($\sim$ 2.8 mm). The fact that the cavities are operated under very cold temperatures puts a limit on how thick the walls could be, not to hinder the cooling process. Stiffening rings are also used for increasing the rigidity of the walls.

13

Lowering the Loaded Q

It is desired to operate the SRF cavity at a high loaded Q factor to achieve very high RF voltages at the eigenfrequency of the cavity, which results in a very narrow bandwidth for operation. Lowering the loaded Q will result in a wider bandwidth, hence operating at the initial RF frequency during the presence of disturbances will not result in a dramatic drop in the voltage level. However the peak magnitude at a lower-Q cavity is much lower than that of a high-Q cavity, therefore increasing the RF power will be required, which again is not cost effective.

Mechanical Compensation

Mechanical compensation is based on the idea of changing the shape of the cavity to indemnify for deformation that result in cavity detuning. Mechanical compensation is typically done using either a fast tuner or a slow tuner or both. In our experiment both kinds of tuners have been used, more detailed discussion will be addressed in Chapter 4.

2.5 Problem Formulation and Preliminary Work

From (2.2), we see that detuning can be reduced by decreasing the phase angle ψ. Towards that end, we develop a model for ψ. Two basic assumptions in developing this model are:

- The system with input u and output ψ is linear and time-invariant. Hence, it can be represented by a transfer function $G(s)$ from u to ψ [12].

- Mechanical vibrations, which affect the cavity in a distributed way, can be modelled by an equivalent lumped disturbance that affects the system at the same point where the control actuator is applied [11, Section 2.7]. In other words, the input to the system can be represented as the sum $u - d$, where d is the disturbance input and u is the control input.

The transfer function $G(s)$ can be determined experimentally by applying a sinusoidal input at u and measuring the steady-state phase angle ψ. Using a lock-in amplifier to sweep the frequency of the sinusoidal input over the frequency band of interest, we can determine the frequency response from the input u to the output ψ, which produces the Bode plots of the transfer function.

From a control theory viewpoint, the problem reduces to designing the control u to reject or attenuate the effect of the disturbance d on the output ψ. Six different control techniques for disturbance rejection have been examined. They are

1. Proportional (P)

2. Proportional-Integral (PI)

3. Proportional-Integral-Derivative (PID)

4. High-gain band-limited

5. Servocompensator design

6. Adaptive Feedforward Cancellation (AFC)

The first four controllers are used for disturbance rejection of a wide class of disturbance inputs. They do not require the disturbance input to have a special form,

15

other than being a bounded signal. The last two techniques work when the disturbance input can be represented as the sum of sinusoidal signals of known frequencies but unknown amplitudes and phases. The six techniques were investigated in the internal reports [13, 18] using simulation of an experimentally-determined model of a single-cell copper RF cavity at room temperature. The simulation studies showed that the traditional P, PI, and PID controllers would not achieve the desired level of disturbance attenuation because the controller gains are limited by stability requirements. In the high-gain band-limited control design, a controller is designed to have a high loop gain over the frequency band of interest, while rolling off the loop's frequency response rapidly at high frequency to ensure the stability of the closed-loop system. In the low-frequency range the controller essentially inverts the system's transfer function, which is allowable in our case because the transfer function is stable and minimum phase. The drawback of this design is the relatively high order of the controller, which may not be justified in view of the fact that such a controller guards against a wide class of disturbance inputs that may not be present in the current problem. It is worthwhile to note that this technique is used by Simrock et al. [19] for microphonics control of a quarter wave resonator with a fast piezoelectric tuner. However, our investigation indicates that the complexity of the controller and the demand on the control effort in such a design will be prohibitive for multi-cell cavities because the order of the controller will be very high. Even in the simple experiment of [19], the controller's order is 20, i.e., the degree of the denominator polynomial of the controller's transfer function is 20.

A common cause of microphonics is mechanical vibrations that are almost periodic; in particular, the disturbance signal can be represented as the sum of a finite number of sinusoidal signals, such as disturbances caused by turning on nearby pumps, motors,...etc. That are not well isolated from ground. For this type of disturbance, the techniques of servocompensators, e.g. [3, 8], and adaptive feedforward cancellation, e.g. [1, 20], are more appropriate because they are designed to work with this particular class of signals. The servocompensator approach includes an internal model of the disturbance signal as part of the controller in such a way that the loop gain at the frequencies of the disturbance is infinite; hence rejecting the disturbance asymptotically. Adaptive feedforward cancellation uses an adaptive algorithm to learn the magnitudes and phases of the sinusoidal disturbances and synthesizes the control to cancel them. Both approaches performed satisfactorily in the simulation study [18], but the AFC has the advantage that the only information about the transfer function $G(s)$ that is needed is its magnitude and phase at the input frequencies, which are easily obtained from the measured Bode plots. We will see in the next section that we can tolerate up to $90\,\mathrm{deg}$ error in determining the phase and that errors in determining the magnitude will affect the speed of convergence of the adaptive algorithm but will not alter its stability. Although [1] showed equivalence between the AFC and a special design of the internal model for the servocompensator approach, we must still obtain an analytic model of the system in the form of a rational transfer function to use in designing the compensator. Because of the simplicity of the AFC method, we have adopted it in the experimental part of our work. The method is explained in more detail in the next section.

CHAPTER 3

Adaptive Feedforward Cancellation

3.1 Introduction

The purpose of this chapter is to introduce Adaptive Feedforward Cancellation (AFC). AFC is a control technique for disturbance attenuation that is based on the comparison of an error signal to an estimated signal, which is adjusted continuously to drive the error asymptotically towards zero. Convergence of the error to zero ensures that the estimated parameters converge to the true ones.

Consider a linear stable system represented by the transfer function $G(s)$. Let y be the output of the system and suppose the input is the sum of two signals $u - d$, as shown in Figure 3.1, where u is the control input and d is an unknown disturbance that
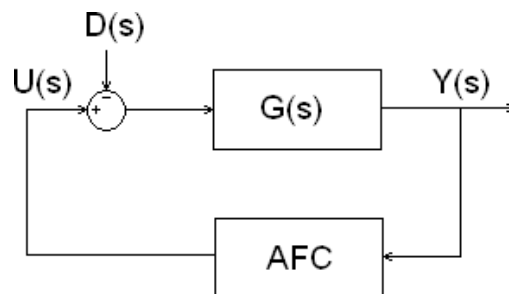
Figure 3.1. Overall system.

can be modelled as the sum of sinusoidal signals of known frequencies, but unknown amplitudes and phases, that is,

$$d = \sum_{i=1}^{n} A_i \sin(\omega_i t + \beta_i) \stackrel{\text{def}}{=} \sum_{i=1}^{n} [a_i \cos(\omega_i t) + b_i \sin(\omega_i t)] \qquad (3.1)$$

in which ω_i, for $i = 1, \cdots, n$, are known but a_i and b_i are unknown.

The controller design will be shown in Section 3.2 using an online adaptive law for parameter estimation. In Section 3.3, analysis supporting the controller design will be shown by following the analysis done in [16, Chapter 4], then some extra work deriving an average model for the system will be demonstrated in Section 3.4. Robustness of the method to uncertainties in the frequencies ω_1 to ω_n will be discussed in the last section.

3.2 Controller Design

The goal is to design the control input so as to attenuate the output y in the presence of the disturbance d. Had we known the amplitudes and phases of the sinusoidal signals, we could have cancelled the disturbance by the control

$$u = \sum_{i=1}^{n} [a_i \cos(\omega_i t) + b_i \sin(\omega_i t)]$$

19

To cope with the uncertainty in the parameters a_i and b_i, we use the control

$$u = \sum_{i=1}^{n} [\hat{a}_i(t) \cos(\omega_i t) + \hat{b}_i(t) \sin(\omega_i t)] \qquad (3.2)$$

where $\hat{a}_i(t)$ and $\hat{b}_i(t)$ are estimates of a_i and b_i, respectively, obtained by the adaptive algorithm [7, Chapter 4]

$$\dot{\hat{a}}_i(t) = -\gamma_i y(t) \cos(\omega_i t + \theta_i) \qquad (3.3)$$

$$\dot{\hat{b}}_i(t) = -\gamma_i y(t) \sin(\omega_i t + \theta_i) \qquad (3.4)$$

for $i = 1, \ldots, n$, where the adaptation gains $\gamma_1, \ldots, \gamma_n$ and the phase advances $\theta_1, \ldots, \theta_n$ are chosen to ensure the convergence of $\hat{a}_i$ and $\hat{b}_i$ to a_i and b_i, respectively. The adaptive algorithm can be rewritten as

$$\dot{z}(t) = -\Gamma y(t) w_a \qquad (3.5)$$

where

$$
z(t) = \begin{bmatrix} \hat{a}_1(t) - a_1 \\ \hat{b}_1(t) - b_1 \\ \hat{a}_2(t) - a_2 \\ \hat{b}_2(t) - b_2 \\ \vdots \\ \hat{a}_n(t) - a_n \\ \hat{b}_n(t) - b_n \end{bmatrix}, \quad w_a = \begin{bmatrix} \cos(\omega_1 t + \theta_1) \\ \sin(\omega_1 t + \theta_1) \\ \cos(\omega_2 t + \theta_2) \\ \sin(\omega_2 t + \theta_2) \\ \vdots \\ \cos(\omega_n t + \theta_n) \\ \sin(\omega_n t + \theta_n) \end{bmatrix}
$$

$$
\Gamma = \text{diag}[\gamma_1, \gamma_1, \gamma_2, \gamma_2, \ldots, \gamma_n, \gamma_n]
$$

It will be shown in section 3.4 that by choosing $\theta_i = \angle G(j\omega_i)$ and choosing γ_i sufficiently small, we can ensure that

$$
\lim_{t \to \infty} z(t) = 0 \tag{3.6}
$$

It will be also shown that we can tolerate up to 90 deg error in determining the phase of the transfer function at ω_i. The limit (3.6) implies that $\lim_{t \to \infty} y(t) = 0$. We can then conclude that the adaptive algorithm ensures convergence of the parameter estimates $\hat{a}_i$ and $\hat{b}_i$ to the true parameters a_i and b_i, respectively, and convergence of the output $y(t)$ to zero.

3.3 Averaging Analysis

We start by expressing w_a in terms of

$$
w = \begin{bmatrix} \cos(\omega_1 t) \\ \sin(\omega_1) \\ \vdots \\ \cos(\omega_n) \\ \sin(\omega_n) \end{bmatrix}
$$

using the trigonometric identities

$$
\cos(\omega t + \theta) = \cos \omega t \cos \theta - \sin \omega t \sin \theta
$$

$$
\sin(\omega t + \theta) = \cos \omega t \sin \theta + \sin \omega t \cos \theta
$$

which can be written in matrix form as

$$
\begin{bmatrix} \cos(\omega t + \theta) \\ \sin(\omega t + \theta) \end{bmatrix} = \begin{bmatrix} \cos \theta & -\sin \theta \\ \sin \theta & \cos \theta \end{bmatrix} \begin{bmatrix} \cos \omega t \\ \sin \omega t \end{bmatrix}
$$

we have

$$
w_a(t) = Ew(t) \tag{3.7}
$$

where

$$E = \text{blockdiag}[E_1, E_2, \ldots, E_n], \quad E_i \stackrel{\text{def}}{=} \begin{bmatrix} \cos\theta_i & -\sin\theta_i \\ \sin\theta_i & \cos\theta_i \end{bmatrix}$$

State-Space Model

Let $\{A, B, C\}$ be a minimal realization of the transfer function $G(s)$. Then, the overall system can be represented in state space as

$$\dot{x}(t) = Ax(t) + B[u(t) - d(t)] \tag{3.8}$$

$$y(t) = Cx(t) \tag{3.9}$$

where

$$
\begin{aligned}
u(t) - d(t) &= \sum_{i=1}^{n}\left[(\hat{a}_i(t) - a_i)\cos\omega_i t + (\hat{b}_i(t) - b_i)\sin\omega_i t\right] \\
&= \begin{bmatrix} \hat{a}_1(t) - a_1 \\ \hat{b}_1(t) - b_1 \\ \hat{a}_2(t) - a_2 \\ \hat{b}_2(t) - b_2 \\ \vdots \\ \hat{a}_n(t) - a_n \\ \hat{b}_n(t) - b_n \end{bmatrix}^T \begin{bmatrix} \cos(\omega_1 t) \\ \sin(\omega_1 t) \\ \cos(\omega_2 t) \\ \sin(\omega_2 t) \\ \vdots \\ \cos(\omega_n t) \\ \sin(\omega_n t) \end{bmatrix} \\
&= z^T(t)w(t)
\end{aligned}
$$

From equations (3.5), (3.7), and (3.9)

$$\dot{z}(t) = -\Gamma y(t)Ew(t) = -\Gamma Ew(t)y(t) = -\Gamma Ew(t)Cx(t) \qquad (3.10)$$

Augmenting (3.10) with (3.8), we obtain the closed-loop model

$$\dot{z}(t) \quad = \quad -\Gamma Ew(t)Cx(t) \qquad\qquad\qquad (3.11)$$

$$\dot{x}(t) \quad = \quad Ax(t) + Bz^T(t)w(t) \qquad\qquad (3.12)$$

System Transformation

Equations (3.11) and (3.12) take the form of [16, equations 4.4.14 and 4.4.15]. We will follow that book in applying averaging. Define

$$\nu(t,z) = \int_0^t e^{A(t-\tau)}Bz^Tw(\tau)d\tau$$

Consider z to be frozen (treated as a fixed parameter), then ν represents the steady-state value of x.

$$\nu(t,z) \quad = \quad \int_0^t e^{A(t-\tau)}Bw^\tau(\tau)d\tau z$$

$$\frac{\partial \nu}{\partial t} \quad = \quad \left[Bw^T(t) + A\int_0^t e^{A(t-\tau)}Bz^Tw(\tau)d\tau \right] z$$

$$\quad = \quad Bw^T(t)z + A\nu(t,z)$$

$$\frac{\partial \nu}{\partial z} \quad = \quad \int_0^t e^{A(t-\tau)}Bw^T(\tau)d\tau \stackrel{\text{def}}{=} \kappa(t)$$

24

Thus, $\nu(t, z) = \kappa(t)z$. Consider now the following change of variables

$$
\begin{aligned}
h &= x - \nu(t, z) \\
\dot{h} &= \dot{x} - \frac{\partial \nu}{\partial t} - \frac{\partial \nu}{\partial z}\dot{z} \\
&= Ax + Bw^T z - Bw^T z - A\nu - \kappa(t)\dot{z} \\
&= Ah + \kappa \Gamma E w(t) C(h + \nu)
\end{aligned}
$$

Let $\varepsilon = \max_i \gamma_i$ and write Γ as

$$
\Gamma = \varepsilon \Gamma_1
$$

where the elements of the diagonal matrix Γ_1 satisfy $\frac{\gamma_i}{\varepsilon} \leq 1$. Then the transformed system can be written as

$$
\dot{z} = -\varepsilon \Gamma_1 E w(t) C[h + \kappa(t)z] \tag{3.13}
$$

$$
\dot{h} = Ah + \varepsilon \kappa(t)\Gamma_1 E w(t) C[h + \kappa(t)z] \tag{3.14}
$$

Averaging Theory

Equations (3.13) and (3.14) take the form of [16, equations 4.4.1 and 4.4.2] with

$$
f(t, z, h) = -\Gamma_1 E w(t) C[h + \kappa(t)z]
$$

$$
g(t, z, h) = \kappa(t)\Gamma_1 E w(t) C[h + \kappa(t)z]
$$

25

Noting that the eigenvalues of A have negative real parts, because $G(s)$ is stable, we conclude from [16, Section 4.4.1] that by choosing the adaptation gains γ_i small enough, $z(t)$ would be much slower than $w(t)$ and $x(t)$ and we can apply the averaging theorem [16, Theorem 4.4.3] to conclude that $z(t)$ can be approximated by the solution of the (time-invariant) average system

$$
\begin{aligned}
\dot{z}(t) &= \varepsilon \lim_{T \to \infty} \frac{1}{T} \int_{t_o}^{t_o+T} f(\tau, z, 0) d\tau \\
&= \lim_{T \to \infty} \frac{1}{T} \int_{t_o}^{t_o+T} [-\Gamma E w(\tau) C \kappa(\tau) z] d\tau \\
&= -\Gamma E \lim_{T \to \infty} \frac{1}{T} \int_{t_o}^{t_o+T} [w(\tau) C \kappa(\tau)] d\tau \ z \\
&= Fz
\end{aligned}
$$

where

$$
\begin{aligned}
F &= -\Gamma E \lim_{T \to \infty} \frac{1}{T} \int_{t_o}^{t_o+T} [w(\tau) C \kappa(\tau)] d\tau \\
&= -\Gamma E \lim_{T \to \infty} \frac{1}{T} \int_{t_0}^{t_0+T} \left\{ w(\tau) C \int_0^\tau e^{A(\tau-\sigma)} B w^T(\sigma) \, d\sigma \right\} d\tau
\end{aligned}
$$

Assuming that F is a Hurwitz matrix (all Eigenvalues have negative real parts), it follows from [16, Theorem 4.4.3] that

$$
\lim_{t \to \infty} z(t) = 0, \quad \lim_{t \to \infty} x(t) = 0
$$

which shows that $\lim_{t \to \infty} y(t) = 0$. We conclude that, in the absence of measurement noise, the adaptive algorithm ensures convergence of the parameter estimates $\hat{a}_i$ and

26

$\hat{b}_i$ to the true parameters a_i and b_i, respectively, and convergence of the output $y(t)$ to zero. In the presence of bounded measurement noise, we can invoke standard perturbation analysis, e.g., [10, Chapter 9], to show that, after finite time, $z(t)$ and $y(t)$ will be of the order of the amplitude of the measurement noise.

3.4   Average Model

By following the analysis of [16], an expression for F has been derived. Now we will carry out some extra computations to further simplify F, obtain conditions under which it will be Hurwitz, and see how error in measurements would affect the conditions for stability. To obtain a general expression for the matrix F, we will start our computations with the case of a disturbance with single frequency component ω_1; then we will carry on with the calculations for the case of two frequencies ω_1 and ω_2, at which point a general formula for multiple frequencies can be easily concluded.

3.4.1   Single Frequency Component

Assume that the disturbance signal has one frequency ω_1. Then,

$$
w(t) = \begin{bmatrix} \cos \omega_1 t \\ \sin \omega_1 t \end{bmatrix}, \quad \Gamma = \begin{bmatrix} \gamma_1 & 0 \\ 0 & \gamma_1 \end{bmatrix}, \quad E = E_1 = \begin{bmatrix} \cos \theta_1 & -\sin \theta_1 \\ \sin \theta_1 & \cos \theta_1 \end{bmatrix}
$$

$$
\begin{aligned}
C\kappa(\tau) &= \int_0^\tau C e^{A(\tau-\sigma)} B w^T(\sigma) \, d\sigma \\
G(s) &= C(sI - A)^{-1} B
\end{aligned}
$$

27

For averaging analysis, $C\kappa(\tau)$ will be taken as the steady-state response of $G(j\omega)$ to the input $w(t)$. Let

$$G(j\omega_1) \;=\; R_1 + jI_1$$

where

$$R_1 \;=\; |G(j\omega_1)|\cos\phi_1 \qquad\qquad (3.15)$$

$$I_1 \;=\; |G(j\omega_1)|\sin\phi_1 \qquad\qquad (3.16)$$

and $\phi_1 = \angle G(j\omega_1)$. Therefore at steady state

$$C\kappa(t) = \Big[\; R_1\cos(\omega_1 t) - I_1\sin(\omega_1 t), \quad I_1\cos(\omega_1 t) + R_1\sin(\omega_1 t) \;\Big] \qquad (3.17)$$

Then $w(t)C\kappa(t)$ will be a 2×2 matrix such that

$$(1,1) \;=\; R_1\cos^2(\omega_1 t) - I_1\sin(\omega_1 t)\cos(\omega_1 t)$$

$$(1,2) \;=\; I_1\cos^2(\omega_1 t) + R_1\cos(\omega_1 t)\sin(\omega_1 t)$$

$$(2,1) \;=\; R_1\cos(\omega_1 t)\sin(\omega_1 t) - I_1\sin^2(\omega_1 t)$$

$$(2,2) \;=\; I_1\cos(\omega_1 t)\sin(\omega_1 t) + R_1\sin^2(\omega_1 t)$$

Since

$$F \;=\; -\Gamma E \lim_{T\to\infty} \frac{1}{T}\int_{t_o}^{t_o+T} [w(\tau)C\kappa(\tau)]d\tau$$

28

$$= -\Gamma E\{w(t)C\kappa(t)\}_{average}$$

we will need to average each element of the $w(t)C\kappa(t)$ matrix. Since

$$\{\sin(\omega_i t)\cos(\omega_i t)\}_{average} = 0 \qquad (3.18)$$

$$\{\sin^2(\omega_i t)\}_{average} = \frac{1}{2} \qquad (3.19)$$

$$\{\cos^2(\omega_i t)\}_{average} = \frac{1}{2} \qquad (3.20)$$

we have

$$\{w(t)C\kappa(t)\}_{average} = \frac{1}{2}\begin{bmatrix} R_1 & I_1 \\ -I_1 & R_1 \end{bmatrix}$$

and

$$
\begin{aligned}
F &= -\Gamma E\{w(t)C\kappa(t)\}_{average} \\
&= -\frac{\gamma_1}{2}\begin{bmatrix} \cos\theta_1 & -\sin\theta_1 \\ \sin\theta_1 & \cos\theta_1 \end{bmatrix}\begin{bmatrix} R_1 & I_1 \\ -I_1 & R_1 \end{bmatrix} \\
&= -\frac{\gamma_1}{2}\begin{bmatrix} R_1\cos\theta_1 + I_1\sin\theta_1 & I_1\cos\theta_1 - R_1\sin\theta_1 \\ R_1\sin\theta_1 - I_1\cos\theta_1 & I_1\sin\theta_1 + R_1\cos\theta_1 \end{bmatrix}
\end{aligned}
$$

From equations (3.15) and (3.16) we see that the elements of F are further simplified to

$$(1,1) = \frac{1}{2}|G(j\omega_1)|\left[\cos\theta_1\cos\phi_1 + \sin\theta_1\sin\phi_1\right]$$

29

$$= \frac{1}{2}|G(j\omega_1)|\cos(\theta_1 - \phi_1)$$

$$(1,2) = \frac{1}{2}|G(j\omega_1)|\left[\cos\theta_1\sin\phi_1 - \sin\theta_1\cos\phi_1\right]$$

$$= \frac{1}{2}|G(j\omega_1)|\sin(\theta_1 - \phi_1)$$

$$(2,1) = \frac{1}{2}|G(j\omega_1)|\left[-\cos\theta_1\cos\phi_1 + \sin\theta_1\sin\phi_1\right]$$

$$= -\frac{1}{2}|G(j\omega_1)|\sin(\theta_1 - \phi_1)$$

$$(2,2) = \frac{1}{2}|G(j\omega_1)|\left[\cos\theta_1\cos\phi_1 + \sin\theta_1\sin\phi_1\right]$$

$$= \frac{1}{2}|G(j\omega_1)|\cos(\theta_1 - \phi_1)$$

Then

$$F = -\frac{\gamma_1}{2}|G(j\omega_1)| \begin{bmatrix} \cos(\theta_1 - \phi_1) & \sin(\theta_1 - \phi_1) \\ -\sin(\theta_1 - \phi_1) & \cos(\theta_1 - \phi_1) \end{bmatrix}$$

The eigenvalues of F are the roots of

$$det(\lambda I - F) = [\lambda + \frac{\gamma_1^2}{4}|G(j\omega_1)|^2\cos^2(\theta_1 - \phi_1)]^2 + \frac{\gamma_1^2}{4}|G(j\omega_1)|^2\sin^2(\theta_1 - \phi_1) = 0$$

which are given by

$$\lambda_{1,2} = -\frac{\gamma_1}{2}|g(j\omega_1)|\cos(\theta_1 - \phi_1) \pm j\frac{\gamma_1}{2}|G(j\omega_1)|\sin(\theta_1 - \phi_1)$$

Hence

$$Re\{\lambda(F)\} = -\frac{\gamma_1}{2}|G(j\omega_1)|\cos(\theta_1 - \phi_1)$$

Choosing θ_1 to satisfy

$$|\theta_1 - \angle G(j\omega_1)| < 90 \deg \tag{3.21}$$

ensures that the eigenvalues of F have negative real parts at $-\frac{\gamma_1}{2}|G(j\omega_1)|\cos(\theta_1 - \phi_1)$.

The best choice would be

$$\theta_1 = \angle G(j\omega_1)$$

which yields multiple real eigenvalues at $-\frac{\gamma_1}{2}|G(j\omega_1)|$. In this case, (3.21) shows that we can tolerate up to $90 \deg$ error in determining the phase of the transfer function at ω_1.

3.4.2 Two Frequency Components

To calculate F with two frequency components present in the disturbance signal, we will go through the same steps as done in section (3.4.1), but with two frequencies.

Consider

$$
w(t) = \begin{bmatrix} \cos \omega_1 t \\ \sin \omega_1 t \\ \cos \omega_2 t \\ \sin \omega_2 t \end{bmatrix}, \quad \Gamma = \begin{bmatrix} \gamma_1 & 0 & 0 & 0 \\ 0 & \gamma_1 & 0 & 0 \\ 0 & 0 & \gamma_2 & 0 \\ 0 & 0 & 0 & \gamma_2 \end{bmatrix}
$$

$$
E = \begin{bmatrix} E_1 & 0 \\ 0 & E_2 \end{bmatrix}, \quad E_i = \begin{bmatrix} \cos \theta_i & -\sin \theta_i \\ \sin \theta_i & \cos \theta_i \end{bmatrix}
$$

Then, at steady state,

$$
C\kappa(t) = \begin{bmatrix} R_1 \cos(\omega_1 t) - I_1 \sin(\omega_1 t) \\ I_1 \cos(\omega_1 t) + R_1 \sin(\omega_1 t) \\ R_2 \cos(\omega_2 t) - I_2 \sin(\omega_2 t) \\ I_2 \cos(\omega_2 t) + R_2 \sin(\omega_2 t) \end{bmatrix}^T
$$

where $G(j\omega_i) = R_i + jI_i$. The 4×4 matrix is given by the following elements

$$
\begin{aligned}
(1,1) &= R_1 \cos^2(\omega_1 t) - I_1 \sin(\omega_1 t) \cos(\omega_1 t) \\[2mm]
(1,2) &= I_1 \cos^2(\omega_1 t) + R_1 \cos(\omega_1 t) \sin(\omega_1 t) \\[2mm]
(1,3) &= R_2 \cos(\omega_1 t) \cos(\omega_2 t) - I_2 \cos(\omega_1 t) \sin(\omega_2 t) \\[2mm]
(1,4) &= I_2 \cos(\omega_1 t) \cos(\omega_2 t) + R_2 \cos(\omega_1 t) \sin(\omega_2 t) \\[2mm]
(2,1) &= R_1 \cos(\omega_2 t) \sin(\omega_1 t) - I_1 \sin^2(\omega_1 t)
\end{aligned}
$$

$$(2,2) = I_1 \cos(\omega_1 t) \sin(\omega_1 t) + R_1 \sin^2(\omega_1 t)$$

$$(2,3) = R_2 \sin(\omega_1 t) \cos(\omega_2 t) - I_2 \sin(\omega_1 t) \sin(\omega_2 t)$$

$$(2,4) = I_2 \sin(\omega_1 t) \cos(\omega_2 t) + R_2 \sin(\omega_1 t) \sin(\omega_2 t)$$

$$(3,1) = R_1 \cos(\omega_2 t) \cos(\omega_1 t) - I_1 \cos(\omega_2 t) \sin(\omega_1 t)$$

$$(3,2) = I_1 \cos(\omega_1 t) \cos(\omega_2 t) + R_1 \cos(\omega_2 t) \sin(\omega_1 t)$$

$$(3,3) = R_2 \cos^2(\omega_2 t) - I_2 \sin(\omega_2 t) \cos(\omega_2 t)$$

$$(3,4) = I_2 \cos^2(\omega_2 t) + R_2 \cos(\omega_2 t) \sin(\omega_2 t)$$

$$(4,1) = R_1 \sin(\omega_2 t) \cos(\omega_1 t) - I_1 \sin(\omega_1 t) \sin(\omega_2 t)$$

$$(4,2) = I_1 \sin(\omega_2 t) \cos(\omega_1 t) + R_1 \sin(\omega_2 t) \sin(\omega_1 t)$$

$$(4,3) = R_2 \cos(\omega_2 t) \sin(\omega_2 t) - I_2 \sin^2(\omega_2 t)$$

$$(4,4) = I_2 \cos(\omega_2 t) \sin(\omega_2 t) + R_2 \sin^2(\omega_2 t)$$

To calculate $\{w(t)C\kappa(t)\}_{average}$ we first need to calculate the averages of cross product terms with two different frequencies. Since these terms are not periodic, we use the generalized form $\lim_{T\longrightarrow\infty} \frac{1}{T} \int_{t_0}^{t_0+T} [f(t)]\, dt$ to calculate the averages.

$\{\cos(\omega_1 t) \cos(\omega_2 t)\}_{average}$

$$
\begin{aligned}
&= \lim_{T\longrightarrow\infty} \frac{1}{T} \int_{t_0}^{t_0+T} [\cos(\omega_1 t) \cos(\omega_2 t)]\, dt \\
&= \lim_{T\longrightarrow\infty} \frac{1}{T} \int_{t_0}^{t_0+T} \frac{1}{2}\{\cos((\omega_1 - \omega_2)t) + \cos((\omega_1 + \omega_2)t)\}dt \\
&= \frac{1}{2}\{\cos((\omega_1 - \omega_2)t) + \cos((\omega_1 + \omega_2)t)\}_{average} = 0 \quad\quad\quad (3.22)
\end{aligned}
$$

$\{\sin(\omega_1 t)\sin(\omega_2 t)\}_{average}$

$$
\begin{aligned}
&= \lim_{T\longrightarrow\infty} \frac{1}{T} \int_{t_0}^{t_0+T} [\sin(\omega_1 t)\sin(\omega_2 t)]\, dt \\
&= \lim_{T\longrightarrow\infty} \frac{1}{T} \int_{t_0}^{t_0+T} \frac{1}{2}\{\cos((\omega_1-\omega_2)t) - \cos((\omega_1+\omega_2)t)\}dt \\
&= \frac{1}{2}\{\cos((\omega_1-\omega_2)t) - \cos((\omega_1+\omega_2)t)\}_{average} = 0 \quad\quad (3.23)
\end{aligned}
$$

$\{\sin(\omega_1 t)\cos(\omega_2 t)\}_{average}$

$$
\begin{aligned}
&= \lim_{T\longrightarrow\infty} \frac{1}{T} \int_{t_0}^{t_0+T} [\sin(\omega_1 t)\cos(\omega_2 t)]\, dt \\
&= \lim_{T\longrightarrow\infty} \frac{1}{T} \int_{t_0}^{t_0+T} \frac{1}{2}\{\sin((\omega_1+\omega_2)t) + \sin((\omega_1-\omega_2)t)\}dt \\
&= \frac{1}{2}\{\sin((\omega_1+\omega_2)t) + \sin((\omega_1-\omega_2)t)\}_{average} = 0 \quad\quad (3.24)
\end{aligned}
$$

Along with Equations (3.18), (3.19) and (3.20), we conclude that

$$
\begin{aligned}
F &= -\Gamma E\{w(t)C\kappa(t)\}_{average} \\
&= -\frac{\Gamma}{2}
\begin{bmatrix}
\cos\theta_1 & -\sin\theta_1 & 0 & 0 \\
\sin\theta_1 & \cos\theta_1 & 0 & 0 \\
0 & 0 & \cos\theta_2 & -\sin\theta_2 \\
0 & 0 & \sin\theta_2 & \cos\theta_2
\end{bmatrix}
\begin{bmatrix}
R_1 & I_1 & 0 & 0 \\
-I_1 & R_1 & 0 & 0 \\
0 & 0 & R_2 & I_2 \\
0 & 0 & -I_2 & R_2
\end{bmatrix} \\
&= \text{blockdiag}\left(-\frac{\gamma_i}{2}|G(j\omega_i)|
\begin{bmatrix}
\cos(\theta_i-\phi_i) & \sin(\theta_i-\phi_i) \\
-\sin(\theta_i-\phi_i) & \cos(\theta_i-\phi_i)
\end{bmatrix}
\right)
\end{aligned}
$$

For i = 1,2. Again by choosing θ_i to satisfy

$$|\theta_i - \angle G(j\omega_i)| < 90 \deg$$

for i = 1,2, we ensure that the eigenvalues of F have negative real parts at $-\frac{\gamma_1}{2}|G(j\omega_1)| \cos(\theta_1 - \phi_1)$ and $-\frac{\gamma_2}{2}|G(j\omega_2)| \cos(\theta_2 - \phi_2)$. The best choice results from taking $\theta_1 = \angle G(j\omega_1)$ and $\theta_2 = \angle G(j\omega_2)$, which ensures that F has real negative eigenvalues at $-\frac{\gamma_1}{2}|G(j\omega_1)|$ and $-\frac{\gamma_2}{2}|G(j\omega_2)|$.

3.4.3 Multiple Frequency Components

Repeating the steps of driving F for single and double frequency components, it can be easily seen that in the general case

$$F = \text{blockdiag}[F_1, F_2, \ldots, F_n]$$

where

$$F_i = -\frac{\gamma_i}{2}|G(j\omega_i)| \begin{bmatrix} \cos(\theta_i - \phi_i) & \sin(\theta_i - \phi_i) \\ -\sin(\theta_i - \phi_i) & \cos(\theta_i - \phi_i) \end{bmatrix}$$

and $\phi_i = \angle G(j\omega_i)$. Choosing θ_i to satisfy

$$|\theta_i - \angle G(j\omega_i)| < 90 \deg \qquad (3.25)$$

35

ensures that the eigenvalues of F_i have negative real parts at $-\frac{\gamma_i}{2}|G(j\omega_i)|\ \cos(\theta_i - \phi_i)$. The best choice would be

$$\theta_i = \angle G(j\omega_i)$$

which yields multiple real eigenvalues at $-\frac{\gamma_i}{2}|G(j\omega_i)|$. In this case, (3.25) shows that we can tolerate up to $90\,\mathrm{deg}$ error in determining the phase of the transfer function at ω_i.

The eigenvalues of F corresponding to different diagonal blocks would vary with the magnitude of the frequency response $|G(j\omega_i)|$. The range of these variations can be limited by choosing $\gamma_i = c_i/|G(j\omega_i)|$ for some positive numbers c_i, which results in eigenvalues at $-\frac{c_i}{2}$, for $i = 1, \ldots, n$. By appropriate choice of the constants c_i, we can have n eigenvalues of the same order of magnitude. It is clear that errors in determining $|G(j\omega_i)|$ will not be crucial, as they affect the location of the eigenvalues of F but do not change the fact that their real parts will be always negative.

The notation used in this chapter is retained in the experimental section, with the exception that the output y is taken to be the phase angle ψ. The state x does not appear in the experimental section as the state model is used only for analysis.

3.5 Robustness to Errors in Modelling the Frequency

In the previous few subsections, the averaging analysis showed that the control algorithm keeps the system stable, and drives the output signal to zero, provided the disturbance frequencies are precisely known. In this section, we use simulation to investigate the effect of having errors in modelling the frequency components of a disturbance. Consider G(s) to be

$$G(s) = \frac{10000}{s^2 + 80s + 10000}$$

and consider the presence of a disturbance signal d, oscillating at $\omega_d = 10$ rad/sec with a magnitude of $1V$ such that

$$d = \sin(10t)$$

The simulation was done on Matlab/Simulink by implementing Equations (3.3) and (3.4) to construct the control signal u as shown in Equation (3.2), and θ is chosen such that $\theta = \angle G(j\omega_u)$, where ω_u is the frequency used for constructing the control signal u, and

$$\omega_u = \omega_d + \Delta\omega$$

Figure 3.2 shows simulation results when the frequency of the disturbance signal

is precisely known. Figure 3.2(a) shows the output y of the system that is desired to be zero. Figure 3.2(b) shows the disturbance signal d that is used throughout the entire simulation, and Figure 3.2(c) shows the output of the system after applying a cancellation signal at a frequency $\omega_u = \omega_d = 10$ rad/sec, which results in driving the phase angle ψ to zero as expected from the foregoing analysis. The control signal u is shown in 3.2(d), while the last figure shows the input to the system $(u-d)$ converging to zero, which means that the control signal u is converging to the disturbance signal d.

Now we will check for the robustness of the system by running different simulations using $\omega_u \neq \omega_d$ (i.e. $\Delta\omega \neq 0$). Figure 3.3 shows results of using a cancellation signal when $\omega_u > \omega_d$ for three different values $\Delta\omega$, while Figure 3.4 shows three more results for $\omega_u < \omega_d$. The left column of plots in Figures 3.3 and 3.4 represent the system's output, y, with an applied control signal, while the right column of plots shows the error between the estimated disturbance signal (control signal) and the actual disturbance signal, i.e., $u - d$.

In Figure 3.3, Plots (a) and (b) show the system's output, y, and the input, $u - d$, respectively using $\omega_u = 11$ rad/sec, Plots (c) and (d) show the case when $\omega_u = 15$ rad/sec, and Plots (e) and (f) show the case when $\omega_u = 50$ rad/sec. In Figure 3.4, Plots (a) and (b) show the case of using $\omega_u = 9$ rad/sec, Plots (c) and (d) show the case when $\omega_u = 5$ rad/sec, and Plots (e) and (f) show the case of using $\omega_u = 1$ rad/sec. It is clear from these figures that the steady-state amplitudes of y and $u - d$ are proportional to small frequency error $\Delta\omega$.
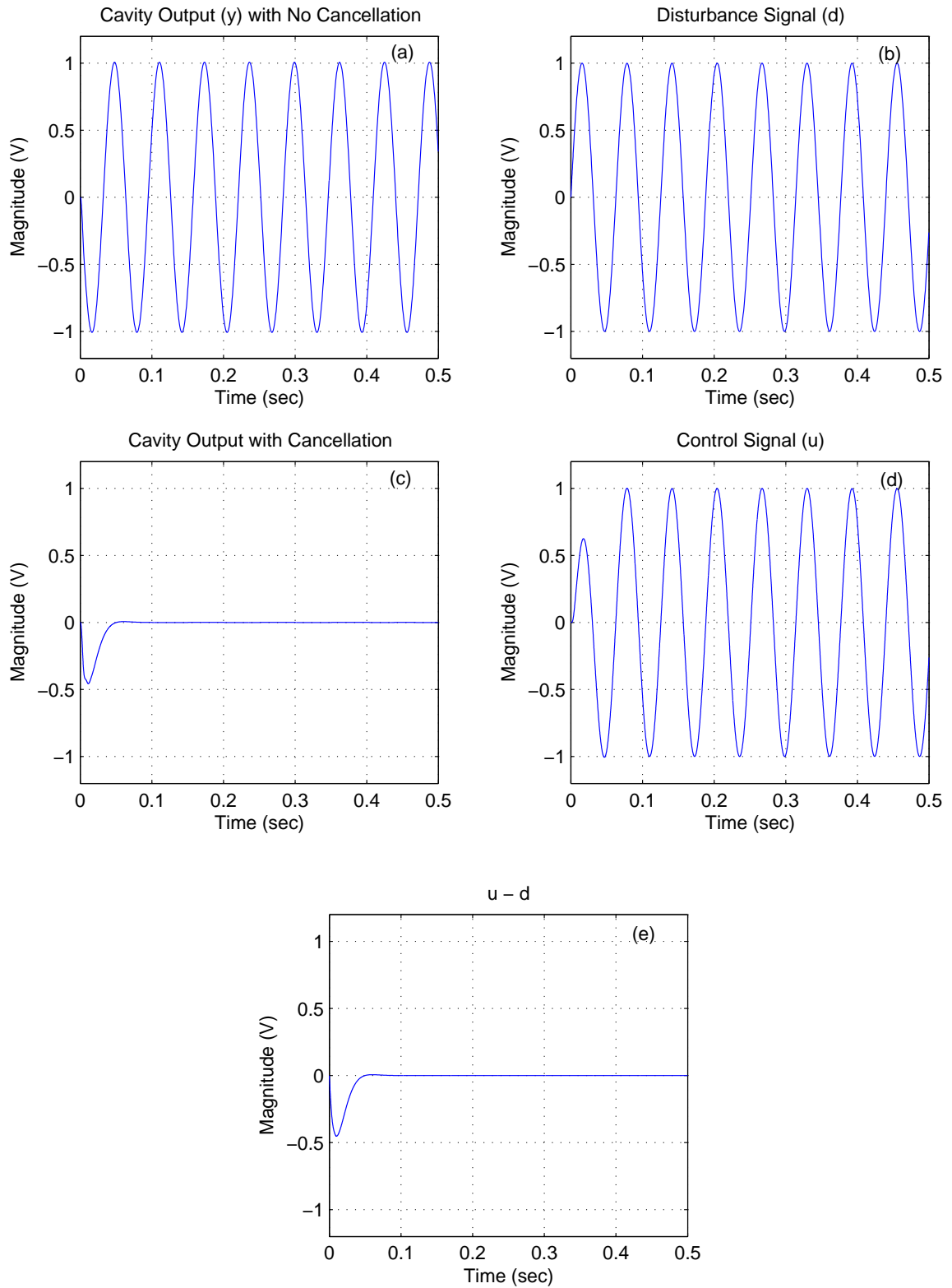
Figure 3.2. Simulation results for disturbance cancellation with a precisely known frequency.
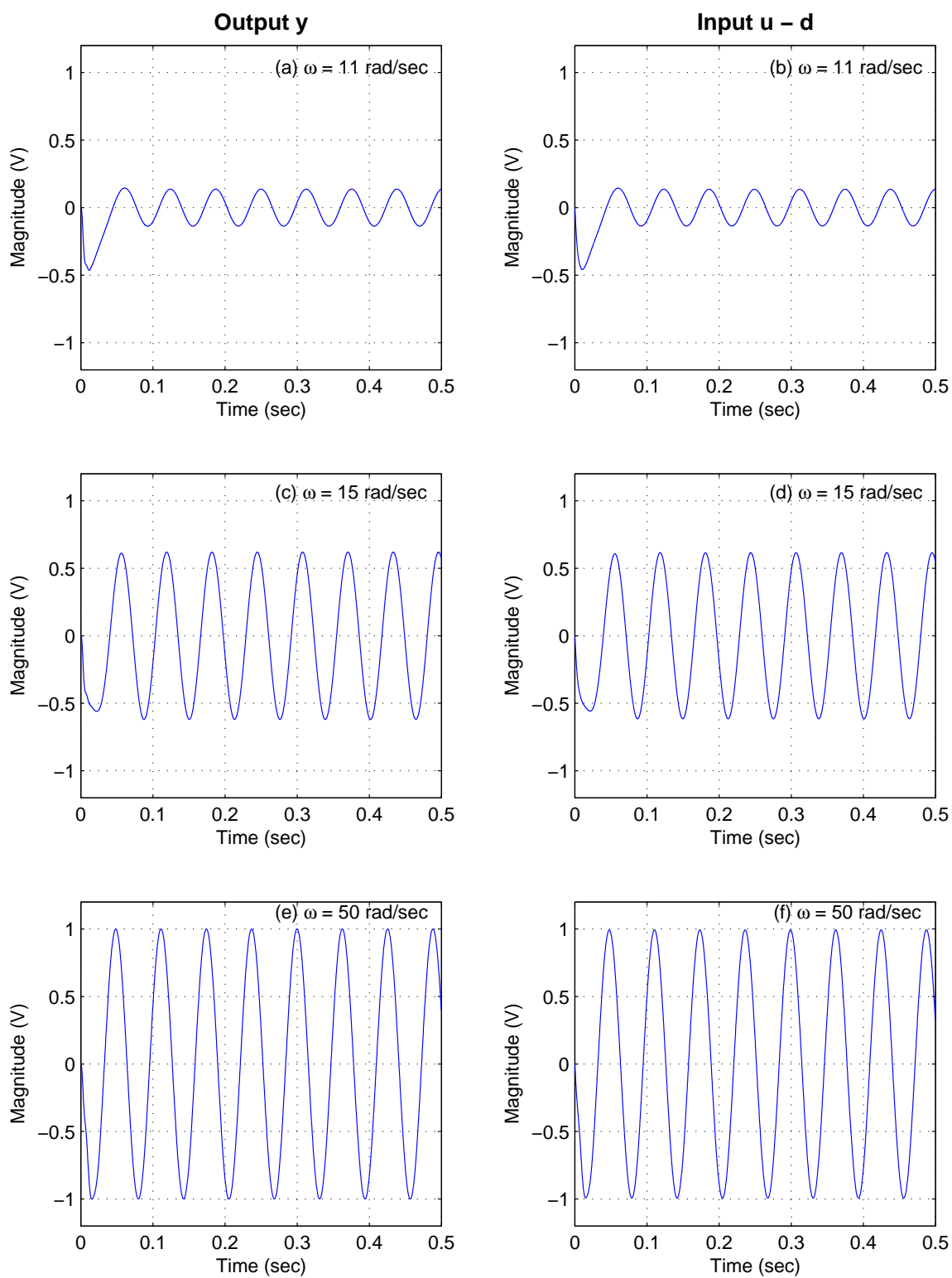
Figure 3.3. Simulation results for disturbance cancellation when $\omega_u > \omega_d$.
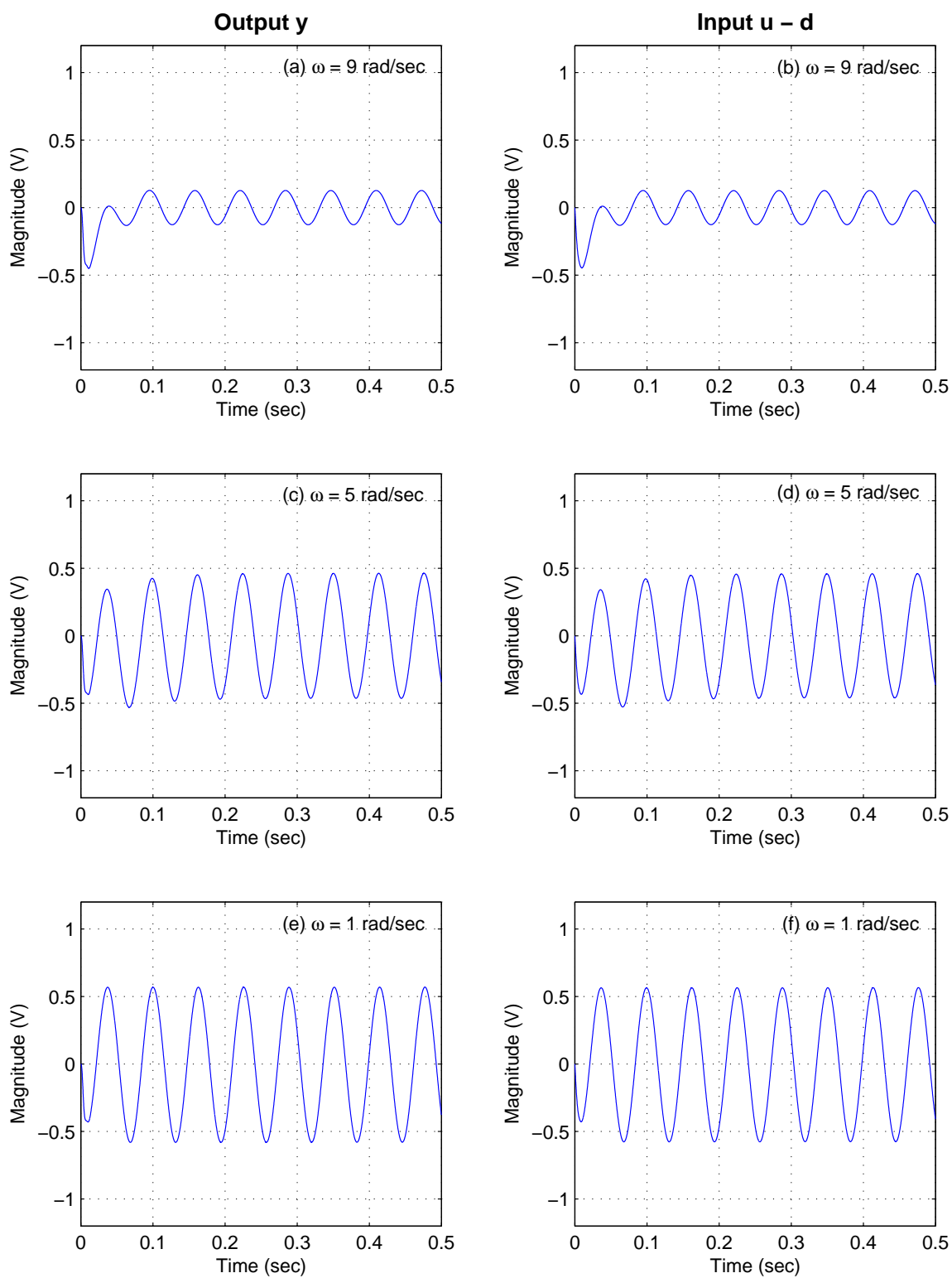
Figure 3.4. Simulation results for disturbance cancellation when $\omega_u < \omega_d$.

41

CHAPTER 4

Microphonics Control

A prototype 805 MHz cryomodule has been tested to demonstrate the required performance for the Rare Isotope Accelerator [4, 5, 9]. The prototype cryomodule has two multi-cell cavities. Figure 4.1 shows the end view and section view of the $\beta = 0.47$ prototype cryomodule, while Figure 4.2 shows the cavities before and after the installation of thermal and magnetic shields. Each multi-cell cavity has an external tuner actuated by a piezoelectric actuator that operates in room temperature for ease of maintenance, while the cavities are cooled down to 2 K under cryoplant temperature regulation. Figure 4.3 shows that the cavity's RF resonance frequency can be tuned using both a coarse (slow) tuner and a fine (fast) tuner (Piezo-electric actuator). The coarse tuner has a linear effect with a span of 1 MHz that is only used at the beginning before operation, by either tightening or loosening on a screw that would push or release some pressure off the tuner rocker arm, which consequently squeezes or relaxes the shape of the cavity, thus tuning the RF resonant frequency within the desired range. The piezo-electric actuator receives a voltage signal from the Adaptive Feedforward controller. For an input range of about 10V, which corresponds to 10 kHz of detuning, the actuator behaves linearly. In the next section, different measurements that have been conducted in preparation for the damping process will be
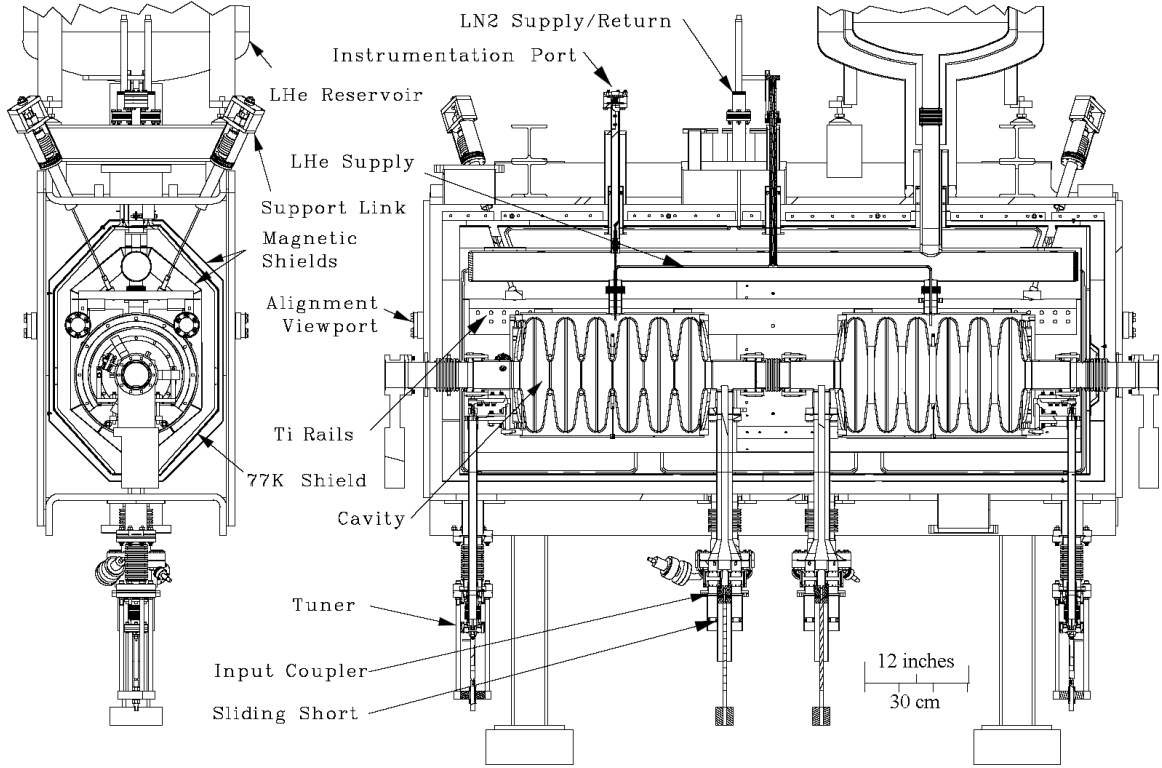
Figure 4.1. End view and section view of the $\beta = 0.47$ prototype cryomodule.

discussed while Section 4.2 shows the experimental setup as well as the results of the cancellation process.

4.1 Measurements

Figure 4.4 shows the experimental setup, where an RF signal generator is used to drive the cavity, through an antenna placed at one terminal of the multi-cell cavity, while another antenna at the other terminal is used to pickup the output signal, where

$$V_{in} = |V_{in}|\sin(\omega_{RF}t + \varphi_{in})$$

$$V_{out} = |V_{out}|\sin(\omega_{RF}t + \varphi_{out})$$

43
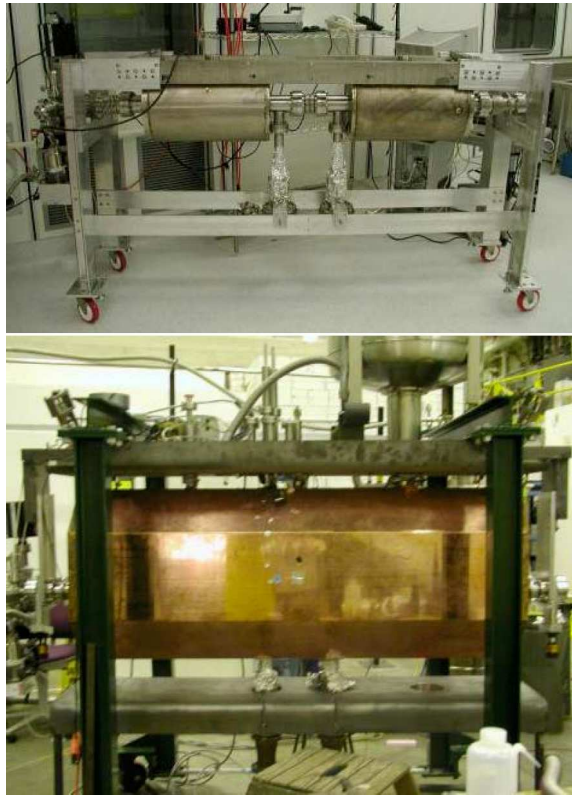
Figure 4.2. Top photo: Cavities inside the helium vessels. Bottom photo: Cold mass after installation of thermal and magnetic shield.

Mechanical
slow tuner

Piezoelectric
fast tuner
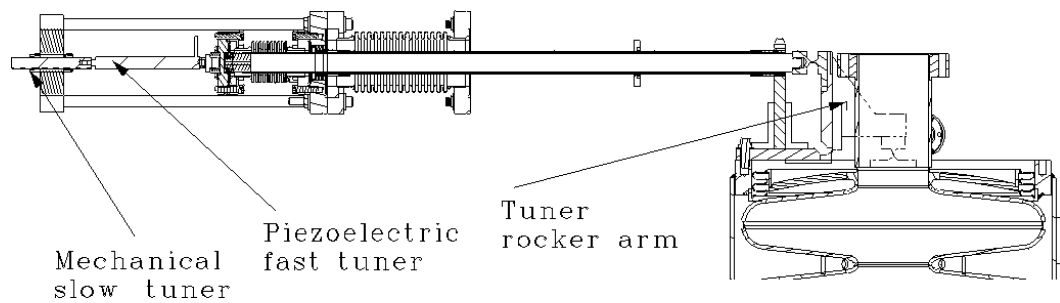
Tuner
rocker arm

Figure 4.3. Position of fine and coarse tuners while attached to the multi-cell cavity.

The signal V_{in} is passed through a phase shifter that compensates for the phase introduced due to cables, probes, and amplifiers and adds a 90° phase shift so that V_{in} would take the form

$$V_{in} = |V_{in}| \cos(\omega_{RF} t + \varphi_{in})$$

These two signals are then mixed together through a mixer to generate a signal containing both the sum and difference of the frequency components of the two mixed signals. The mixer's output is passed through a low pass filter to obtain the low frequency component signal, which is proportional to the cavity detuning through the relation given by equation (2.2). This setup provides us with a real time error signal that is analyzed by different methods to obtain

1. Frequency response of the system (Bode Diagram)

2. Frequency components present in the signal due to disturbances (FFT)

3. Disturbance cancellation using AFC

which will be discussed in detail in the next three subsections.

4.1.1 Bode Diagram

For some physical systems, the structure of the model and its parameters can be easily determined using laws of physics, properties of materials, etc. In many other cases, the plant model and parameters have to be obtained by identification experiments, namely, observing the response of the system to known inputs. If the system
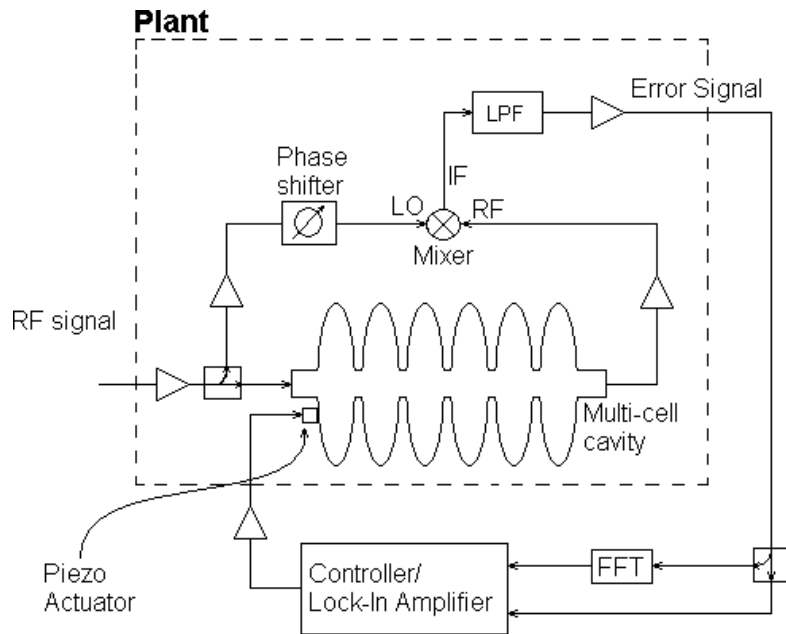
Figure 4.4. Physical setup of the cavities with the control unit or lock-in amplifier.
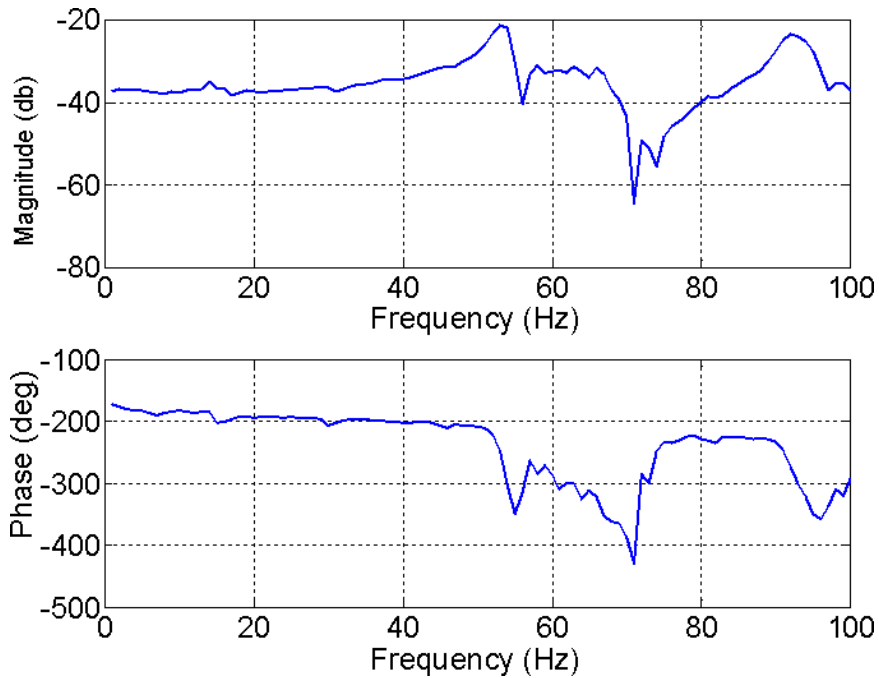

Figure 4.5. The range of interest of the frequency response (Bode diagram) for the system.

parameters are fixed then one can easily derive an analytical model that can be used with different control techniques. But our plant parameters are not fixed; they keep changing quite often that the plant model might change from one day to another, due to changes in operating conditions, pressure, temperature, etc, which makes it hard to model the plant by a fixed transfer function. As mentioned earlier, one of the advantages of the Adaptive Feedforward Cancellation algorithm is its independence on an analytical model for the plant. However, knowing the frequency response of the system at the disturbance frequency ensures stability as shown in chapter 3, and speeds up the disturbance cancellation process as well. Figure 4.5 shows the Bode diagram that has been used in the cancellation process. Although the actual Bode diagram was measured from 1 Hz to 1000 Hz with a phase rolling down to about $-3500\,\mathrm{deg}$, Figure 4.5 only illustrates the range of interest where disturbances have been observed. The Bode diagram was generated from a lock-in amplifier that sends a sinusoidal signal to the piezo-electric actuator through an amplifier. This signal is swept through the desired range of frequencies, step size, and sampling rate, then the error signal is fed back into the lock-in amplifier to be compared to the swept sinusoidal signal and produce a frequency response (Bode diagram) of the system. This process is done off-line, simply by replacing the controller by the digital lock-in amplifier. The data is then saved in the form of a look-up table, from which the phase and magnitude values that correspond to the disturbance frequencies are used as inputs to the controller for better response.

An analytical model (transfer function) of the Bode diagram shown in Figure 4.5 can be approximated by the following 14th order transfer function, which is obtained

Table 4.1. Numerator and denominator coefficients for the modelled transfer function.

Num coeff	Coeff values	Den coeff	Coeff values
α_1	2152	β_1	1
α_2	1.644e005	β_2	130.4
α_3	2.146e009	β_3	1.265e006
α_4	1.375e011	β_4	1.381e008
α_5	8.84e014	β_5	6.678e011
α_6	4.563e016	β_6	5.966e013
α_7	1.925e020	β_7	1.915e017
α_8	7.499e021	β_8	1.349e019
α_9	2.339e025	β_9	3.228e022
α_{10}	6.105e026	β_{10}	1.687e024
α_{11}	1.502e030	β_{11}	3.207e027
α_{12}	1.97e031	β_{12}	1.107e029
α_{13}	3.987e034	β_{13}	1.741e032
		β_{14}	2.982e033
		β_{15}	3.987e036

by trial and error,

$$G(s) = -0.01\ e^{(-0.001\ s)} \left(\frac{\alpha_1 s^{12} + \alpha_2 s^{11} + \ldots + \alpha_{12} s^1 + \alpha_{13}}{\beta_1 s^{14} + \beta_2 s^{13} + \ldots + \beta_{14} s^1 + \beta_{15}} \right) \tag{4.1}$$

where the numerator (num) and denomenator (den) coefficients (coeff) are given in Table 4.1. The transfer function (4.1) has 6 second-order zeroes, and 7 second-order poles whose parameters are shown in Table 4.2. This model is only derived to show the complexity of the system's transfer function and how the changing nature of the parameters of the plant will make it hard to keep modelling the transfer function. Figure 4.6 shows the actual Bode diagram obtained experimentally using a lock-in amplifier, along with the Bode diagram calculated from the transfer function (4.1).

Table 4.2. Parameters for second-order poles and zeroes of the modelled transfer function.

| Poles' center frequencies (rad/sec)	Corresponding damping ratios	Zeroes' center frequencies (rad/sec)	Corresponding damping ratios
333	0.018	351.86	0.0128
364.4	0.0137	370.71	0.0202
383.3	0.0365	389.56	0.03
395.84	0.0299	408.4	0.0208
414.69	0.0145	446.1	0.0022
452.39	0.0111	464.96	0.0107
578	0.0299		
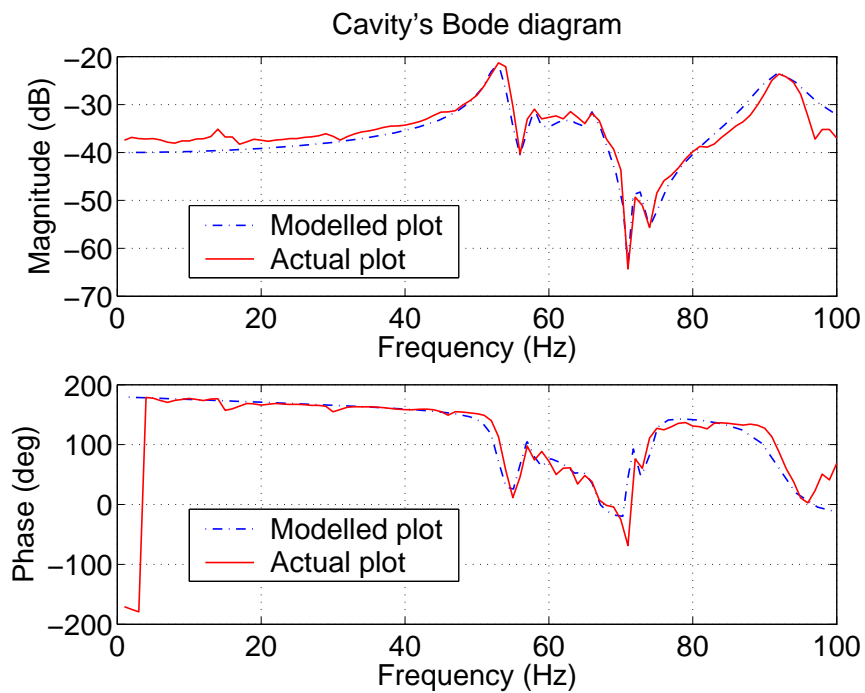
Figure 4.6. A comparison between the actual and the modelled Bode diagrams.

4.1.2 Fast Fourier Transform

The cavity frequency shifts due to vibrations and pressure fluctuations that could deform the cavity walls. Typical sources of vibration are

1. Fluid fluctuation

   - Boiling

   - Cavitation

   - Turbulent flow

2. Rotating machinery

   - Motors

   - Pumps

3. Ground motion

The disturbances caused from fluid fluctuation and rotating machinery are typically narrow band sinusoidal disturbances, while those generated from ground motion are usually broadband vibrations. A properly designed accelerator only exhibits limited narrowband sources of noise, while ground motion should have negligible effect because of adequate ground insulation of the cryomodule. The mechanical frequencies of concern are usually low, less than 200 Hz. In our experiments, the observed disturbances were only below 100 Hz.

Figure 4.7 shows the frequency domain of the RF error signal at three different instances. Instances (a) and (b) take place at the final stage of the cooling process,
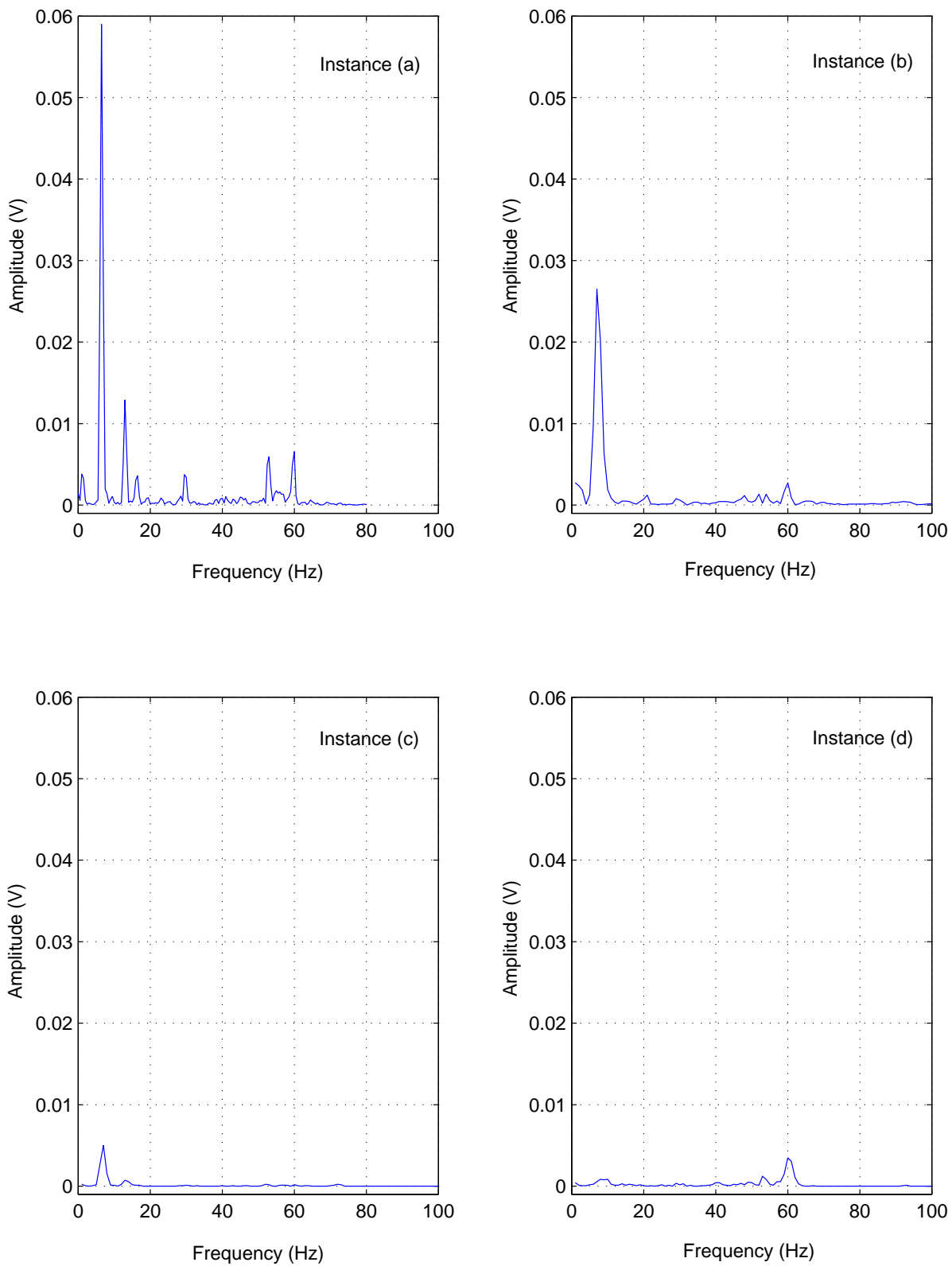
Figure 4.7. FFT of RF error signal at four different instances.

where liquid helium is introduced rapidly filling a helium reservoir to cool the cavities down. Once the helium reservoir is filled, thermo-acoustic oscillations appear at about 6.5 Hz due to trapped gas volumes in the liquid helium space, sometimes this disturbance appears along with its second harmonic as shown at instance (a). These oscillations at 6.5 Hz start decreasing in magnitude as the helium level decreases, allowing the release of trapped gas volumes, and this is shown throughout instances (a), (b) and (c). It is worthwhile mentioning that these oscillations will not be present under normal operating conditions, as the helium reservoir will be empty. Instance (d) takes place after the helium reservoir has been emptied and the thermo-acoustic oscillations are no longer present. We can see that at instance (d) the main source of disturbance is at about 60 Hz, in addition to a small peak at 54 Hz, which most probably corresponds to some rotating machines. It is noticed that the magnitude of the disturbance at 60 Hz varies at different instances, which suggests the possibility of having more than one driving term, rotating at close frequencies, and thus causing frequency beating. Indeed by zooming in onto the 60 Hz, we observed the presence of two components causing that disturbance, one at 59.5 Hz and the other at 59.7 Hz. By taking floor measurements using an accelerometer, and by tracking the signals, the sources were identified to be two cryoplant screw compressors. The accelerometer's readings assured that there are two disturbances one at 59.5 Hz and the other at 59.7 Hz as shown in Figure 4.8. The cryoplant was designed to cool superconducting magnets, and no isolation from the floor or piping were done as vibration was not an issue.
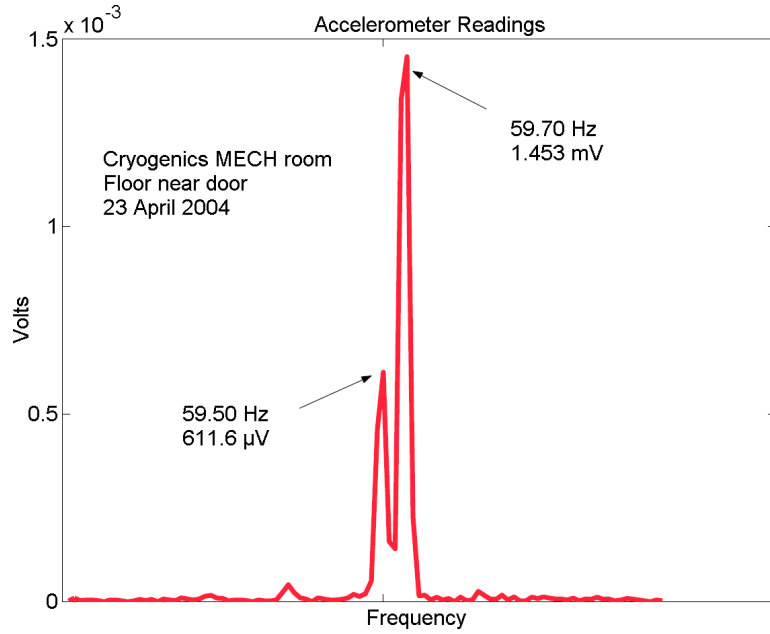
Figure 4.8. Accelerometer measurements near the beating sources.

4.1.3 Calibration

In this subsection, we start by using an example of a mechanical disturbance to have a better understanding of how to relate the RF error signal to the cavity detune, and how to interpret the information obtained from the FFT as to how far does the eigenfrequency of the SRF cavity shift. Then, the calibration measurement that was done for this particular experiment will be discussed.

The RF error signal contains all of the needed information on how the vibrations affect the cavity's RF resonant frequency. The magnitude of the error signal corresponds to how far does the RF resonant frequency ω_o shifts off resonance. Let us consider the following example for clarification. Assume that we have a nearby pump operating at 60 Hz that is not well isolated from the floor, which would act as a mechanical disturbance. The error signal (detuning) will then be a sinusoidal

53

signal of frequency 60 Hz, i.e., $\Delta\omega = \mathrm{M}\sin\left((2\pi \times 60\mathrm{t}) + \varphi\right)$. This will cause the RF resonance frequency (ω_o) to oscillate between $(\omega_o + M)$ and $(\omega_o - M)$ at 60 Hz.

Calibration measurements were done to relate the error signal to the frequency deviation using a Voltage Network Analyzer (VNA) in the continuous wave (cw) mode. The error signal was centered around 0 V with a peak voltage of about 75 mV and the RF signal was swept over a band of 200 Hz centered at the resonance frequency, corresponding to ± 100 Hz of frequency detune, i.e., for this experiment a disturbance signal of a peak voltage of 100 mV causes the RF resonant frequency to detune from ω_o by ± 100 Hz.

4.2 Experimental Demonstration

As shown in Figure 4.4, the estimated noise signal is added to the system by directly shaking an SRF 6-cell elliptical cavity, cooled to 2K, using a piezo-electric actuator (PI, model P-842.60). The controller can also be replaced by a lock-in amplifier to generate the Bode plot of the system.

The block diagram of the AFC algorithm is shown in Figure 4.9 for the case of a single-frequency disturbance. It is an implementation of Equations (3.2), (3.3) and (3.4).

In Figure 4.9, ω is the angular frequency of the disturbance signal that is calculated from an FFT of the RF error signal, θ is a phase advance introduced to ensure maximum stability of the system, and γ is the adaptation gain. Both θ and γ are determined from a measured Bode diagram, where θ is the phase at the frequency to
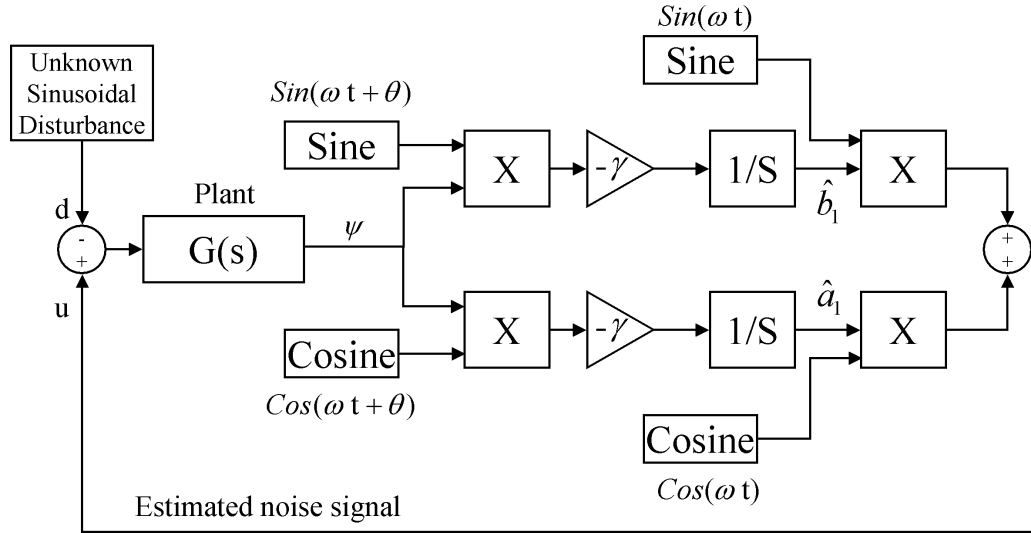
Figure 4.9. Implementation of the AFC on Simulink.

be cancelled and γ, as discussed in Chapter 3, can be calculated from the magnitude information such that its value is large at small magnitudes and relatively small at large magnitudes.

4.2.1 Experimental setup

An external PC is used for modelling the controller in MATLAB/Simulink, which is then built in dSPACE CONTROLDESK developer version that communicates with an external hardware (dSPACE RTI1104 board), with 16 I/O ports. The user's interface is through dSPACE CONTROLDESK developer version for real-time adjustment of the variable parameters.

The setup for obtaining the Bode diagram was discussed earlier in Section 4.1.1 using a lock-in amplifier (SRS digital lock-in amplifier model SR850). The FFT of the RF error signal is generated from the LeCroy Waverunner LT342 digital oscilloscope,

55
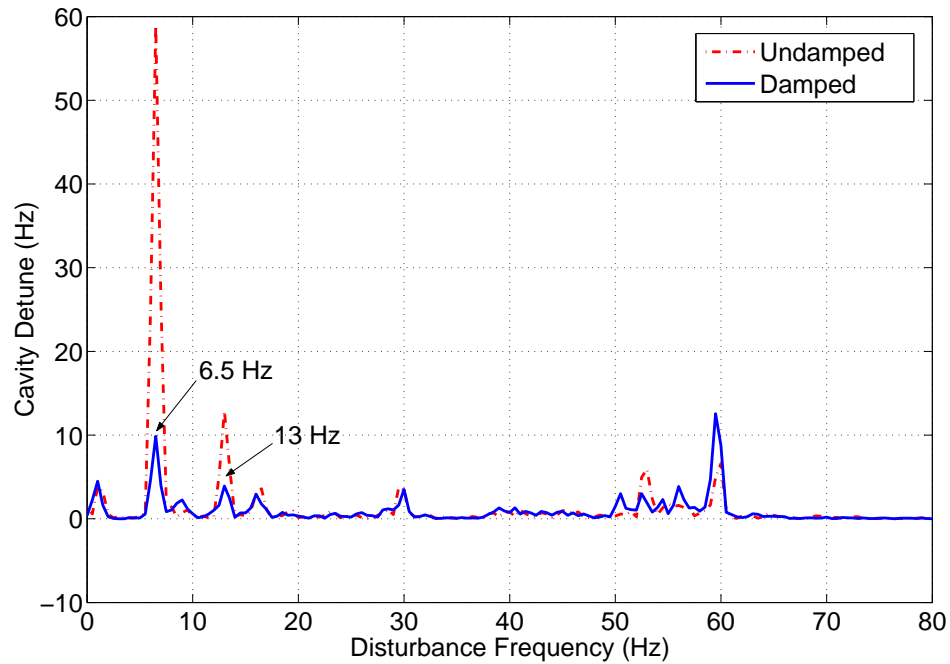
Figure 4.10. Active damping of helium oscillations at 2K.

from which the largest frequency components are picked for damping to acceptable levels.

4.2.2 Experimental Results

We observed two types of microphonics vibration: internal (helium oscillations) and external (motors, pumps, etc.). The results of applying AFC to both types are shown in Figures 4.10 and 4.11.

Figure 4.10 shows an FFT of the detuning for the undamped and damped responses of thermo-acoustic oscillations that was addressed in Section 4.1.2. During this experiment the effect of the oscillation at 6.5 Hz was accompanied with its second harmonic at 13 Hz. After applying a cancellation signal at 6.5 Hz, the effect of
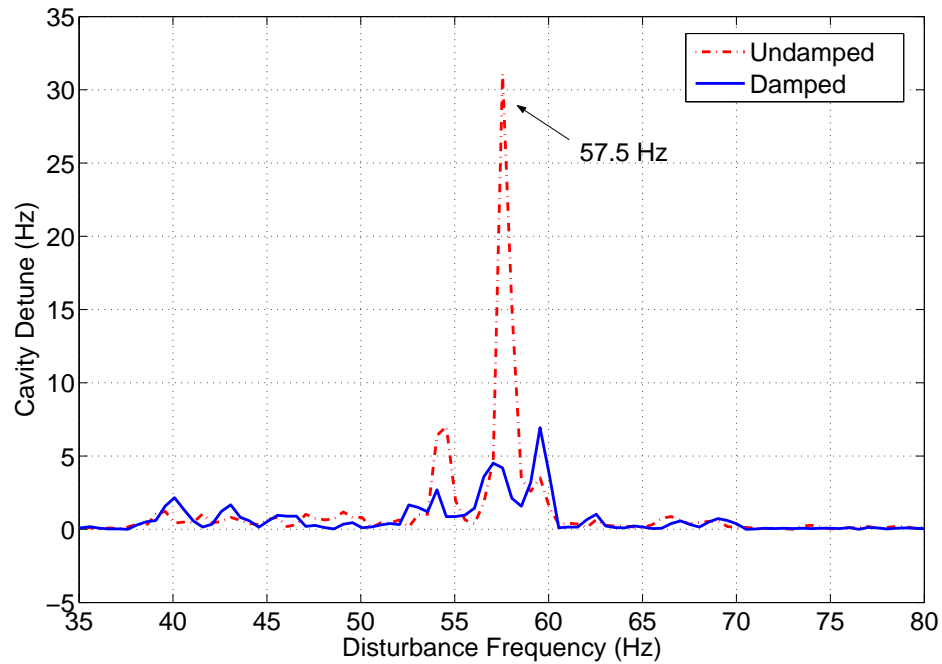
Figure 4.11. Active damping of external vibration at 2K.

the oscillation was damped at that frequency; however the internal energy causing this oscillation was still present, and its effect was observed to have shifted up to the oscillation's second harmonic at 13 Hz increasing the disturbance at that frequency, where another cancellation signal was applied. The first peak at 6.5 Hz was reduced by a factor of 6 from a cavity detune of 59 Hz to 10 Hz, while the second peak at 13 Hz was reduced to a cavity detune of 4 Hz. These oscillations will not be present under the operating conditions as mentioned before. However, testing the active damping for different kinds of disturbances was done to check the performance of the control algorithm.

Figure 4.11 shows the undamped and damped responses due to external vibration from a motor that was turned on purposely for demonstration. The noise appeared

at 57.5 Hz, and it was successfully damped by a factor of 7.4 from a cavity detune of

31 Hz to 4.2 Hz.

CHAPTER 5

Conclusion

A microphonics control algorithm has been developed to control the microphonics problem opposing the particle acceleration process through 6-cell SRF niobium cavity. It is the prototype for a possible RF control system for the Rare Isotope Accelerator project. The adaptive feedforward cancellation (AFC) controller has been implemented at the National Superconducting Cyclotron Laboratory at Michigan State University (E. Lansing, MI, USA). The challenge is to design and develop an RF control that handles disturbances present during continuous wave operation of superconducting cavities. Since Lorentz forces have very small effects on detuning during continuous wave operation, detuning is mainly caused by microphonics.

To date, there has been no demonstration of microphonics control on multi-cell SRF cavities, and the current work presents the first such demonstration, where we have demonstrated the successful use of piezo-electric actuators and the adaptive feedforward cancellation control to damp sinusoidal disturbances due to microphonics in SRF cavities. In the next step, a digital low level radio frequency (LLRF) controller has to be demonstrated working in conjunction with the adaptive feedforward cancellation on the SRF cavities, where the AFC control would attenuate the cavity detune down to low levels such that the LLRF controller could handle. The LLRF would

then apply further cancellation by controlling the RF driving signal of the cavity by continuously adjusting the RF amplitude and phase to maintain a steady output signal that meets the desired amplitude with zero phase.

BIBLIOGRAPHY

BIBLIOGRAPHY

[1] M. Bodson, A. Sacks, and P. Khosla. Harmonic generation in adaptive feedforward cancellation schemes. IEEE Trans. Automat. Contr., 39:1939-1944, 1994.

[2] A. Brinkmann et. al. 1999 Proc. 9th Workshop on RF Superconductivity ed B Rusnak, paper TUA007.

[3] E.J. Davison. The robust control of a servomechanism problem for linear time-invariant multivariable systems. IEEE Trans. Automat. Contr., AC-21(1):25-34, January 1976.

[4] T.L. Grimm, S. Bricker, C. Compton, W. Hartung, M. Johnson, F. Marti, R.C. York, G. Ciovati, and P. Kneisel. Experimental study of an 805 MHz cryomodule for the Rare Isotope Accelerator. In Proceedings of the 2004 International Linear Accelerator Conference, pages 827-829, Lübeck, Germany, 2004.

[5] T.L. Grimm, W. Hartung, T. Kandil, H. Khalil, J. Popielarski, J. Vincent, and R.C. York. Measurement and control of microphonics in high loaded-Q superconducting rf cavities. In Proceedings of the 2004 International Linear Accelerator Conference, pages 815-817, Lübeck, Germany, 2004.

[6] W. Hartung, C.C. Compton, T.L. Grimm, R.C. York, G. Ciovati, P. Kneisel. Status report on multi-cell superconducting cavity development for medium-velocity beams. In Proceedings of the 2003 Particle Accelerator Conference, Portland, Oregon, 2003.

[7] P.A. Ioannou and J. Sun. Robust Adaptive Control. Prentice-Hall, Upper Saddle River, New Jersey, 1996.

[8] A. Isidori, L. Marconi, and A. Serrani. Robust Autonomous Guidance: An Internal Model Approach. Springer, London, 2003.

[9] T.H. Kandil, T.L. Grimm, W. Hartung, H.K. Khalil, J. Popielarski, J.Vincent, and R.C. York. Adaptive Feedforward Cancellation of Sinusoidal Disturbances in Superconducting RF Cavities. In Proceedings of the 2004 International Linear Accelerator Conference, pages 473-475, Lübeck, Germany, 2004.

[10] H.K. Khalil. Nonlinear Systems. Prentice Hall, Upper Saddle River, New Jersey, 3rd edition, 2002.

[11] H. Kwakernaak and R. Sivan. Linear Optimal Control Systems. John Wiley and Sons, Inc., New York, NY, 1972.

[12] L. Lije, S. Simrock, D. Kostin, and M. Fouaidy. Characteristics of a fast piezo-tuning mechanism for superconducting cavities. In 2002 European Particle Accelerator Conference, pages 2256-2258, Paris, 2002.

[13] I.H. Makhdoom. Modeling of superconducting RF cavity voltage and active control of microphonics detuning. Technical report, Michigan State University, East Lansing, MI, USA, 2002.

[14] H. Padamsee, The Science and Technology of Superconducting Cavities for Accelerators. Superconductor science and technology, 14:R28R51, 2001.

[15] H. Padamsee, J. Knobloch, and T. Hays. RF Superconductivity for Accelerators. John Wiley and Sons, Inc., New York, NY, 1998.

[16] S. Sastry and M. Bodson. Adaptive Control. Prentice-Hall, Englewood Cliffs, New Jersey, 1989.

[17] T. Schilcher. Vector sum control of pulsed accelerating fields in Lorentz force detuned superconducting cavities. PhD thesis, University of Hamburg, Hamburg, Germany, 1998.

[18] S. Seshagiri. Active control of microphonics detuning. Technical report, Michigan State University, East Lansing, MI, USA, 2003.

[19] S. Simrock, G. Petrosyan, A. Facco, V. Zviagintsev, S. Andreoli, and R. Paparella. First demonstration of microphonic control of a superconducting cavity with a fast piezoelectric tuner. In 2003 Particle Accelerator Conference, pages 470-472, Portland, OR, 2003.

[20] B. Wu and M. Bodson. Multi-channel active noise control for periodic sources-indirect approach. Automatica, 40:203-212, 2004.